ABSTRACT

Title of thesis: TRANSMISSION ELECTRON MICROSOPY STUDIES
                     OF FEGA ALLOYS

                     Nobuko Koda, Master of Science, 2003

Thesis directed by: Professor Manfred Wuttig
                     Department of Materials Science and Engineering

Microstructural analysis of rapid-solidified (melt-spun) FeGa alloys with

17.3at.%Ga and bulk alloys with 12-20at.%Ga using transmission electron

microscope was carried out. Dark field and high resolution image analysis show

all the samples are inhomogeneous with fine texture of 5-10nm. Although the

expected crystal structure is bcc for all the samples, bulk samples with 12-20at.%-

Ga contain additional phases other than bcc phase. Tetragonal modulation of DO_3

and superlattice with diagonal arrangement of two B2(CsCl-type) cells in bcc

gave the best identification for observed diffraction patterns. Tetragonality

calculated from mismatch between observed diffraction spots and the calculation

for the assumed tetragonal structure was approximately 1.1.

TRANSMISSION ELECTRON MICROSOPY STUDIES OF FEGA
ALLOYS

by

Nobuko Koda

Thesis submitted to the Faculty of the Graduate School of the
University of Maryland, College Park in partial fulfillment
of the requirement for the degree of
Master of Science
2003

Advisory committee:

Professor Lourdes Salamanca-Riba
Dr. James Cullen
Assistant Professor Ichiro Takeuchi

DEDICATION

To

Dr. Shin-ichi Kitahata

who provided an everlasting motivation to study.

SPECIAL ACKNOWLEDGEMENTS

The author wishes to express special acknowledgements for

Dr. Mikio Kishimoto

Mr. Norio Koda
Ms. Kiyoka Koda

Takeshi Kasajima
Kazuko Kasajima

and

Tetsunori Koda

Acknowledgements

Table of Contents

List of Table

List of Figures

List of Negative Identification Numbers of TEM pictures

1. Introduction

1.1. FeGa Alloys

The magnetostriction and elasticity of Fe-based alloys have also been reported. In particular, the greater part of FeAl system has been investigated in 1958 [1]. $Fe_{1-x}Al_x$ system has a disordered B2 structure in the Fe-rich (x<0.20) region and an ordered DO_3 structure around x=0.25[2]. *Hall* reported that saturation magnetostriction of FeAl alloys increases dramatically with atomic percent of Al[3, 4]. The subsequent studies show that the saturation magnetostriction reaches a maximum and shear modulus shows minimum near 25at%Al, whose structure is Fe_3Al[5-7]. It had also been reported that the Al composition dependence of the lattice constant could be associated with atomic arrangements and ordering effects in the region of Fe_3Al[1].

Recently, a large magnetostriction in FeGa has been reported [8-12]. Figure1.1 shows the phase diagram of the Fe-Ga system[2]. Similar to FeAl, FeGa system has DO_3 and other phases around 25at.% Ga and disordered B2 phase below 20at.% [2, 3, 12, 13]. The magnetostriction of FeGa alloys shows similar Ga-concentration (<20at.%) dependence to the Al-concentration dependence of FeAl, but is larger by factor of two. Both show a maximum at around 17at.% [14]. This trend corresponds with a drop in the value of the C_{11}-C_{12} shear elastic constant with increasing Ga or Al concentration [15]. Note that a microscopic explanation of the martensitic transformation is based on the lattice instability due to the softening of the {110}<1$\bar{1}$0> shear modulus ($C'=(C_{11}-C_{12})/2$) of the body-centered cubic high temperature phase[16]. The decrease of magnetostriction at higher Ga concentration is reported to coincide with the change of the structure from the

disordered A2 phase to ordered DO_3 phase[8], [17]. These suggest that the crystal structure of FeGa alloy correlates with both elastic constants and magnetostriction.

1.2. Microstructures

Some of the origins of magnetstriction or elasticity are detected in microscopic analysis. Transmission electron microscope studies on martensitic deformations have been performed for various Fe-based materials[18]. In FePt alloys it was found that the reduction of the elastic constant C' corresponded to a resistance to the $\{110\}<1\bar{1}0>$ shear, also it is quite reasonable that reduction of C' is directly connected with fcc-bcc transformations. The tweed contrast was observed over all the area of the fcc matrix in FePt alloys[19, 20]. In the fcc-hcp transformation of FeMnC, the existence of random stacking faults in both phases was identified by streaks accompanying the spots [21]. The streak appearing in electron diffraction spots is explained by the modulation of crystal arrangement because each diffraction spot corresponds to one 'real' plane therefore includes the information of 'real' shape[22]. In other words, lamellar structures could be confirmed by analyzing the streak of diffraction spots.

Similar observation has been performed in FePd alloys. The tweed structure along <110> direction with 4-10nm width was observed in Fe-Pd30at.% alloy. In addition to that, from high-resolution images of transmission electron microscope analysis it was concluded that the origin of the tweed structure could be attributed to local tetragonal distortions associated with small coherent fct embryos embedded in the fcc[23]. Moreover, the lattice softening was found to play an important role in the formation of the fct embryos[23-25].

Transmission electron microscope analysis for Fe-Be19at.% shows that this alloy has a two-phase microstructure consisting of B2-ordered particles ~5nm in diameter aligned along <100> in the bcc matrix [26]. Since the scale of this phase separation is very small, the two-phase parent of bcc+B2 twinned homogeneously along {112}<111> . Similarly, the elastic softening with respect to twinning was observed in InTl[27].

1.3.   Purpose of this work

The purpose of this work is to probe the microstructure of FeGa alloys and to correlate this with the crystal structure, elastic properties, and magnetoelastic properties. Previous work for various magnetostrictive and elastic materials suggests that there is a strong correlation between magnetostriction/elasticity and microstructure. In order to do this, crystal structure and microstructure of melt-spun samples and bulk samples with different compositions were investigated by analyzing the diffraction patterns and the high-resolution transmission electron microscope images.
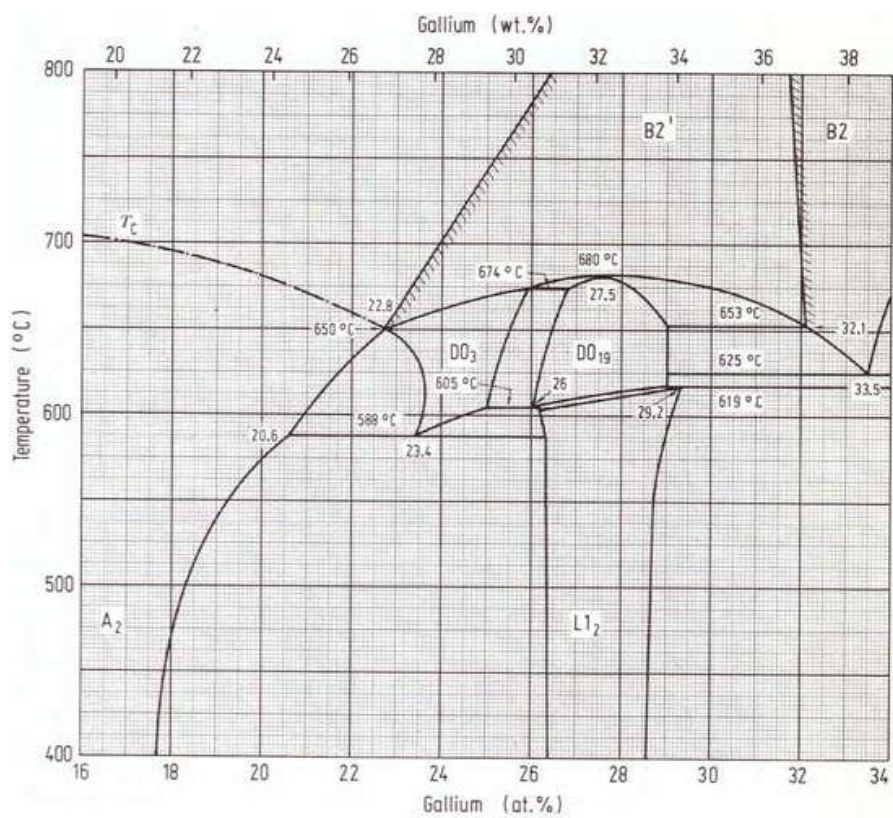
Figure 1.1 Phase Diagram of FeGa in Fe-rich region

2. **Samples**

2.1.   **Rapid-Solidified FeGa Alloys**

An extremely large magnetostriction of 400×10^{-6} is observed in rapid-solidified

(melt-spun) FeGa samples. *Furuya* and *Okazaki* reported that these samples have

columnar grains along the thickness direction and this results in strong anisotropy[11]. In

addition to that, grain boundary character distributions and pole figure analysis show that

the concentration of <001> orientations, which is a magnetic easy axis of the crystal, is

intensive in annealed samples[28, 29]. They concluded that these phenomena produce a

remarkable giant magnetostriction in melt-spun samples. Furthermore, it has been

reported that the melt-spun samples have {100}<011>-type texture with a rotation of

<100> axis from the ribbon normal of about 20º. Also, x-ray diffraction analysis was

concluded that as-spun sample is (310) textured [17].

Melt-spun samples investigated in this work are listed in Table 1-a). All the samples

were prepared by the electromagnetic nozzelless melt spinning method. A schematic of

the system is shown in Figure 2.1[11]. Alloy ingots of Fe-Ga17.3at.% were prepared by

arc-melting high-purity(99.9%) elements and homogenized at 1173K for 24 hours in

vacuum of 10^{-4}Torr. Then small pieces ($5 \times 4 \times 1$mm^3) cut from the ingots were melted and

ejected onto a copper wheel. Samples M-2 and M-3 were annealed at 400ºC for 1hour

under a magnetic fields of 2kOe and 6kOe, respectively, in the ribbon plane direction.

The thickness of the each sample ~30µm and columnar grains along the thickness were

observed using a laser optical microscope [28]. The x-ray diffraction pattern agrees with bcc(A2) structure, which is the expected crystal structure for this composition[2].

2.2.   Bulk FeGa Alloys

Bulk samples used in this work are listed in Table 1-b). All the samples were prepared by the Bridgeman method and sectioned from the ingot[8, 9, 30]. The sectioned samples were annealed at 1000 C for 4 hours under an argon atmosphere in a quartz tube and quenched in water.

The expected crystal structures are bcc for all those samples. However, according to the phase diagram (Figure1.1), $L1_2$ and DO_3 are also possible for sample B-4 (20at.%Ga) depending on the quenching condition[31, 32]. In fact, the x-ray diffraction spectrum shows evidence of the DO_3 structure in Fe-Ga19at.% bulk samples[30]. Furthermore, with reference to $DO_3 \leftrightarrow$ B2 transformation in Fe_3Al, B2 (CsCl-type) structure could also be assumed for calculation in this work[1, 7].
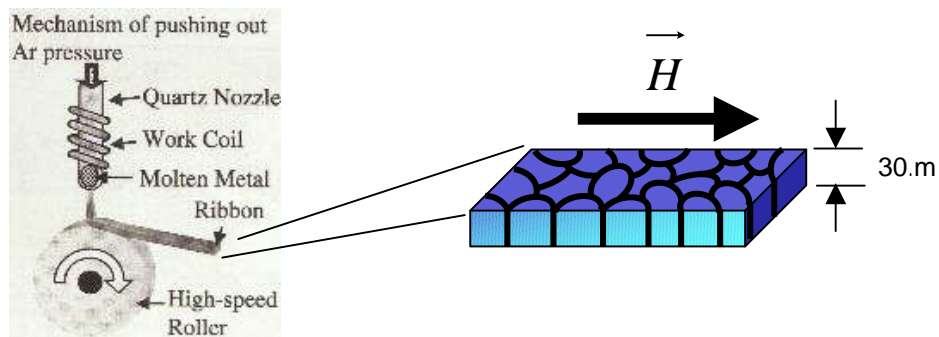

Figure 2.1   Schematic figure of melt-spinning sample preparation

Table 1   List of samples
a)   Melt-spun samples, Ga-17.3at.%

TEM sample #	Annealing condition	Field kOe	Observed direction	Expected crystal structure
M-1	-	-	In-plane	bcc
M-2	400°C,1h	2	In-plane	bcc
M-3	400°C,1h	6	In-plane	bcc
M-4			Cross-sec	bcc

b)   Bulk samples, annealed at 1000C4h, water quenched

TEM sample#	Ga at.%	Field kOe	Expected crystal structure
B-1	12	-	bcc
B-2	14	-	bcc
B-3	16	-	bcc
B-4	20	-	bcc, (L1$_2$,DO$_3$)

( ) … possible structure

3. Experimental Method

3.1.   Sample Preparation for TEM

Figure 3.1 shows the flow chart of the sample preparation method used in this report. Bulk samples were sliced from the original sample along (100)-plane using EDM. The thickness of the slice was 0.5mm. Then the slice was cut into a tetragon shape with sides 2, 2 and 0.5 mm. The samples were then ion milled and mechanically polished to thin the samples to electron transparency. Bulk samples were stuck onto an L-shape holder, and mechanically polished with diamond lapping paper on their square faces to make their thickness under 30µm.

Melt-spun samples were cut into 2mm×2mm squares for observations. Polishing was not used for in-plane samples because these samples were already thin enough for to be milled. For the cross-sectional measurement, a piece of the melt-spun sample was stuck in between two pieces of FeGa crystal, and polished on both sides.

Each of those thinned sample was glued to a 3mm diameter copper grid with 0.8mm diameter aperture, using M-bond 610 epoxy (curing at 150ºC for 1h was required). After that, each sample was mounted onto a rotating stage and ion-milled. In this way, a hole was formed around the center of the aperture of the grid. This took about an hour for melt-spun samples, and several hours for bulk samples. Thickness of the samples around the holes was assumed to be thin enough for the electron beam to transmit.

3.2.TEM Observation

Prepared samples were mounted on the sample stage of a JEOL 4000FX high-resolution transmission electron microscope. Crystal structures were identified by diffraction pattern analysis using EMS On Line [33]. Lattice parameters and interplanar distances were calibrated with a <111> spot in {011}-diffraction of Si single crystal [34].

Melt-spun samples

Bulk samples

30μm

2mm

Slice a piece from bulk

Mechanical polish

Wax

Stick on holder

Polish on lapping paper

Height adjust

3mm 0.8mm

sample

Lapping paper

Copper grid

glue

Glue a grid

Cure

cure

FeGa

Ion milling

Vacuum chamber
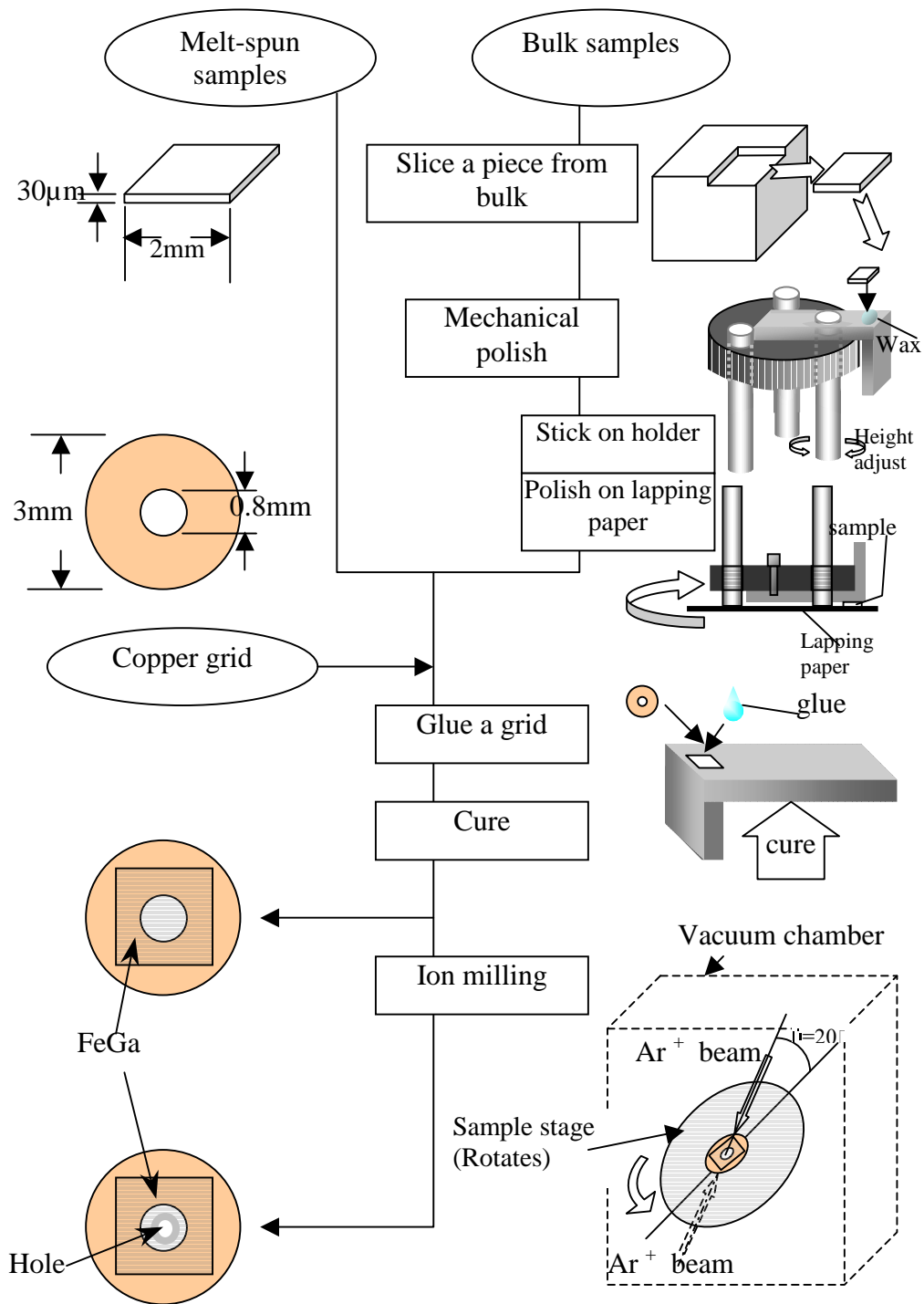
Ar⁺ beam

i=20

Sample stage (Rotates)

Hole

Ar⁺ beam

Figure 3.1 Flow chart of TEM sample preparation

4. Results

4.1. Melt-spun samples, Fe-Ga17.3at.%

Selected area diffraction patterns analysis indicates that the as-spun sample is randomly oriented and does not have any major preferred orientations. On the other hand, the annealed sample has a major diffraction pattern of {001} and the crystal structure was identified as the A2(bcc) structure with a lattice parameter of 0.29nm.

Figure 4.1-a) shows typical diffraction patterns for sample M-3. This pattern is identified as overlap of a {001}-zone axis and close-to-{111}-zone axis. Figures 4.2 to 4.4 are taken from same area of the same sample. Figures 4.2 and 4.3 are dark field images taken with one of the <110> spots in the{001}-diffraction (circle) and in the {111}-diffraction (square) in figure 4.1, respectively. This means that bright area in Figure 4.2 corresponds to the diffraction from the (110)-planes therefore the right half of the selected region has {111} orientation, and the other half has an orientation that is slightly rotated from {001}. This is consistent with the polycrystal feature reported in [11]. Here, Figures 4.1-b) and c) are taken with the selected area of left and right half, respectively, in Figures 4.2 and 4.3. Figure 4.4 shows a dark field image with one of the <200> spots in the{001}-diffraction (triangle). Figures 4.3 and 4.4 are taken with the same diffraction planes, but they show different fine textures.

Fine textures with feature size of 5-10nm are observed in Figures 4.2-4.4. This indicates that these grains are not homogeneous because if the sample is perfectly homogeneous and oriented in one direction, no contrast should appear in the dark field

images of the sample. In order to find out the origin of this texture, high-resolution image of some of the textures in the melt-spun sample were taken and are shown in Figure 4.5. The width of the picture corresponds to 30nm. Black and white contrast corresponds with the microtextures observed in Figures 4.2 and 4.3. Two types of lattice interplanar distances Δ_1 and Δ_2 are observed in this picture. Those spacings correspond to interplanar distances Δ_1 and Δ_2 are calculated to be 0.30 ± 0.01 nm and 0.56 ± 0.02 nm, respectively, where the errors originate from the width of the lines of the arrays in the picture.

4.2.   Bulk , Fe-Ga12-20at.%

Figure 4.6 shows the (001) diffraction patterns for samples B-1(12at.%Ga) to B-4(20at.%Ga). Despite the fact that no other structure other than the bcc-structure is expected for 20at.% sample at any temperature under the melting temperature, Figure 4.6 coincides with the diffraction pattern of B2 or DO_3 structure [2]. Figure 4.7 shows the dark field images corresponding to the diffraction spots A<200>, B<110> and C<100> of sample B-4. Strong contrast appeared in A and B with very weak contrast in C. This suggests that the origin of the spot C is different from A or B. Thus, it is safe to say that this sample has the bcc-structure and some other structure, possibly DO_3. This indicates that this sample has at least two phases and its bcc phase is inhomogeneous.

Other diffraction patterns were observed and are shown in Figure 4.8. These patterns are similar to (013)-diffraction patterns of a B2-structure, but this doesn't explain all of the spots that appear in figure 4.8. These same diffraction patterns were also observed in other bulk samples.

Dark field images of the diffraction spots labeled D, E and F in Figure 4.8 are shown in Figure 4.9-D,E and F, respectively. All of these images are similar to <001> in figure 4.7. Thus, it is possible to say that these spots have same origin, but it is difficult to confirm this because the intensity of the image (distribution of this phase to total amount) is too weak. Other bulk samples show similar images corresponding to D,E and F.

The same series of observations were done for other samples. Dark field images of sample B-1 and B-2 with A<110>, B<200> and C<100> are shown in Figure 4.10 and 4.11. In order to discuss a correlation between magnetostriction and microstructure, dark field images with <200> in the {100}-diffraction of all the samples are shown in Figure 4.12 [12].

Figure 4.1 Diffraction patterns of annealed melt-spun sample M-3. (a) typical diffraction patterns (b) taken with the selected area of left and (c) right half in figure 4.2. <110> in {001}(circle), <110> (square) and <200>(triangle) in {111}

Calculated {001}-diffraction
pattern of bcc (or B2 disordered)
structure.

Calculated {111}-diffraction
pattern of bcc (or B2 disordered)
structure.
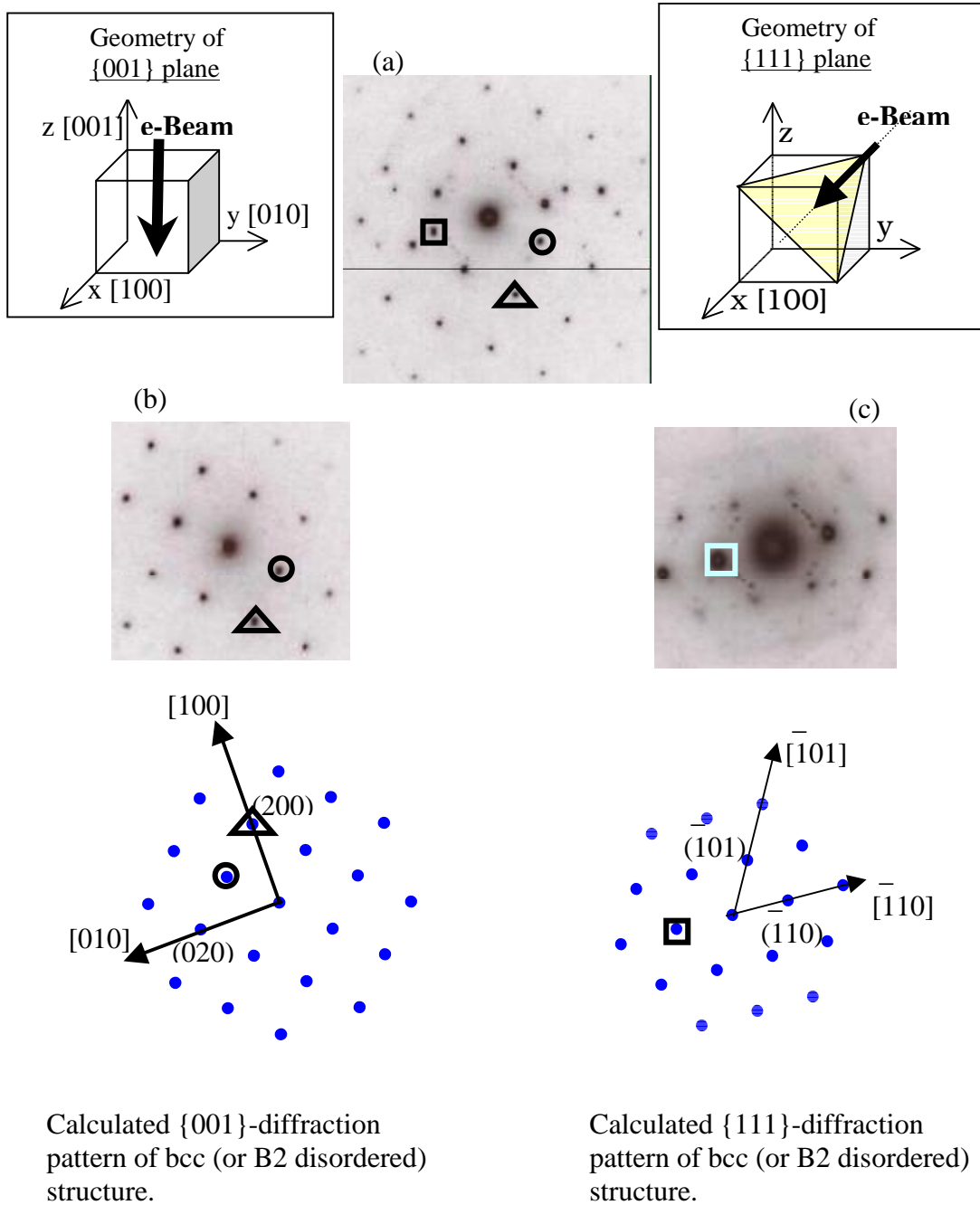
Figure 4.2   Dark field images of (001)-(111) grain boundary with
<110>in{111}(square in Figure 4.1)
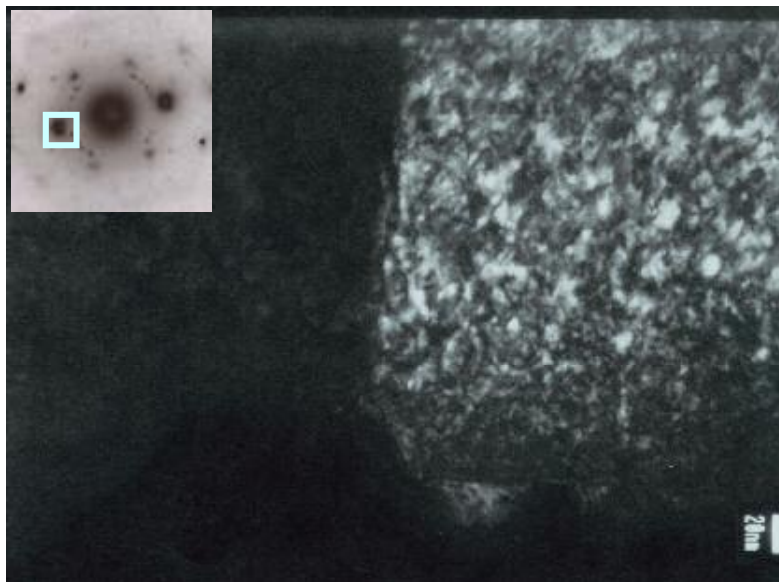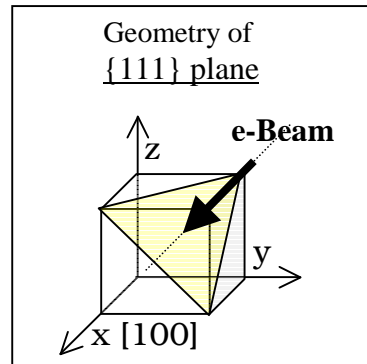
Figure 4.3   Dark field images of (001)-(111) grain boundary
with <110>in{001}(circle in Figure 4.1)

Geometry of
{001} plane
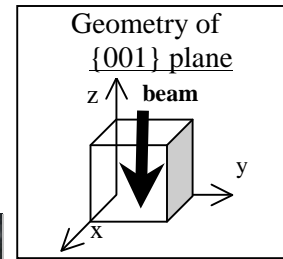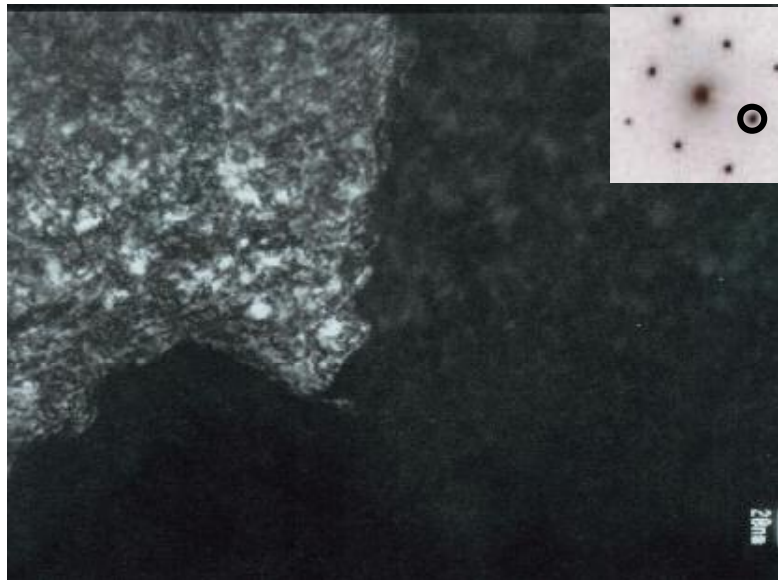
Figure 4.4   Dark field images of (001)-(111) grain boundary with
<200>in{001}(triangle in Figure 4.1)
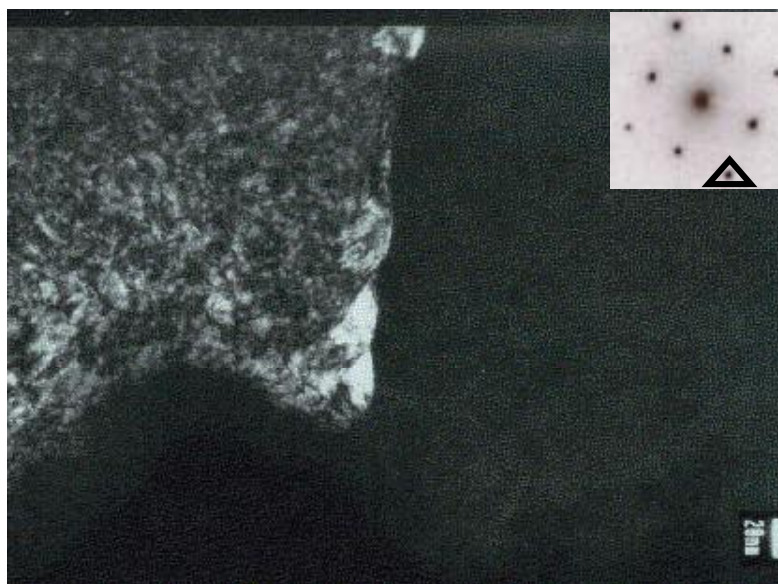
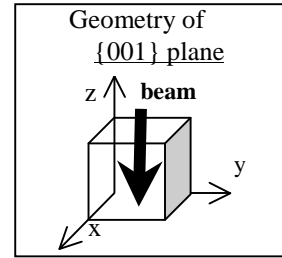Figure 4.5   High resolution image of melt-spun sample. Width of picture=30nm

3nm
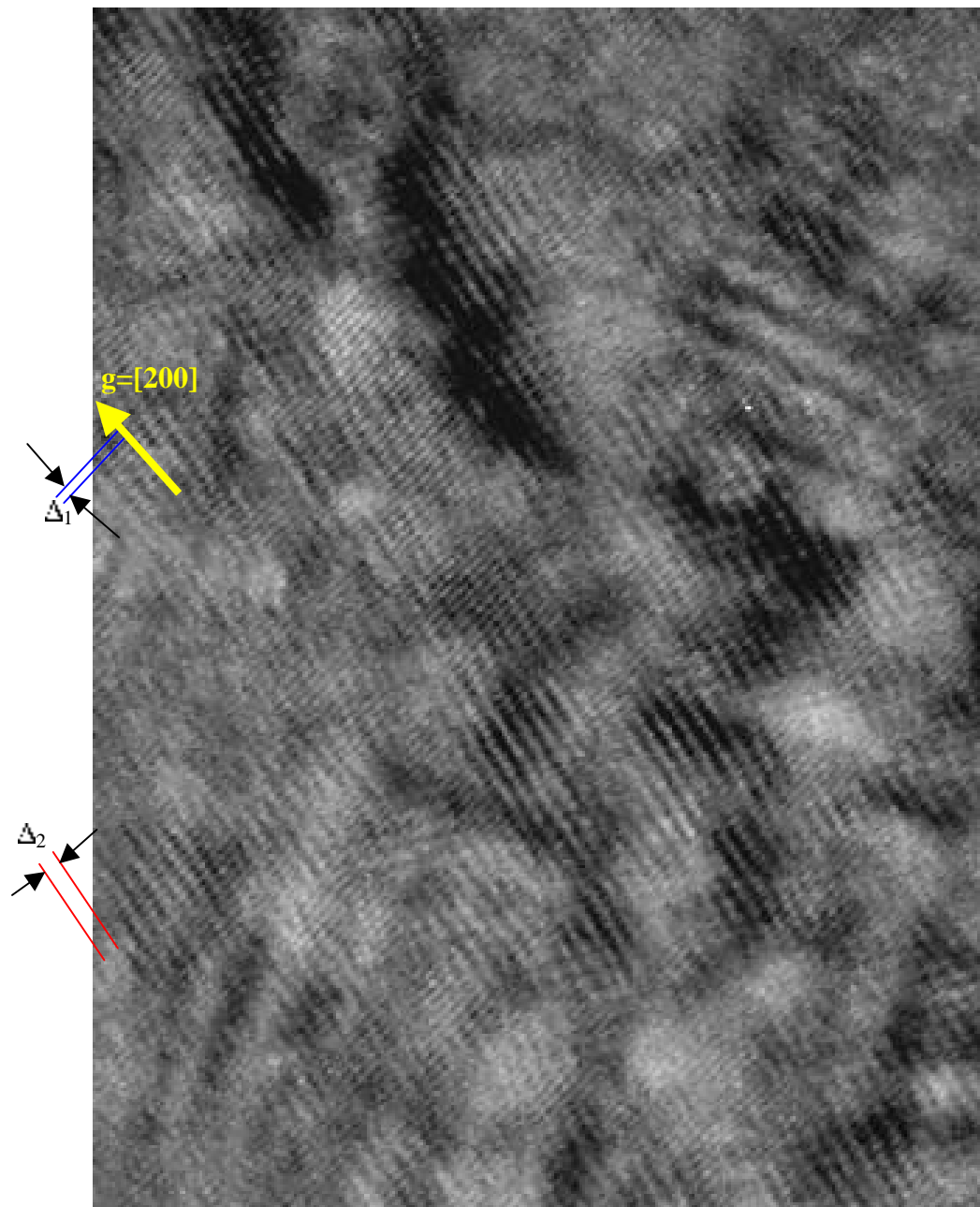
Δ_1= 0.30 nm ± 0.01 (width of lines)
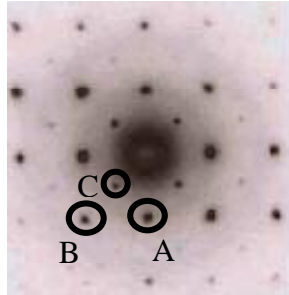Δ_2= 0.56 nm ± 0.02 (width of lines)

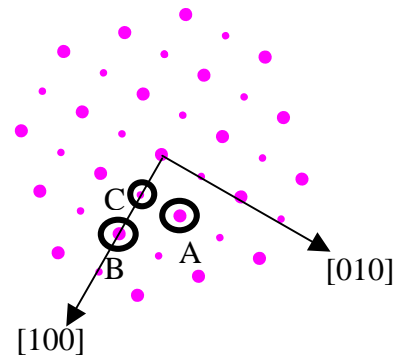Figure 4.6 (001)-diffraction patterns of bulk samples.
 A:[110], B[200] and C:[100].
■ : bcc, • + ■: B2.

Geometry of
{001} plane

z   beam

y

x

20at.%Ga

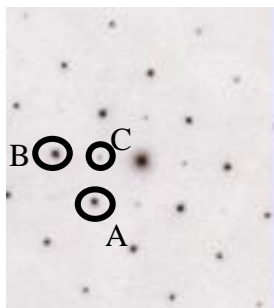[100]   [010]

14at.%Ga

[010]

[100]

12at.%Ga

[100]

[010]
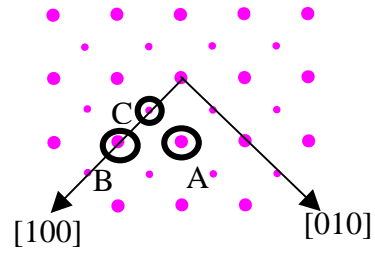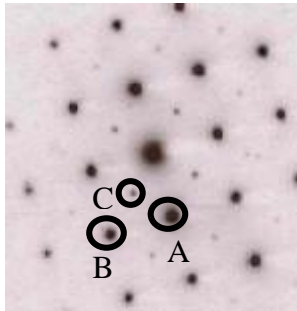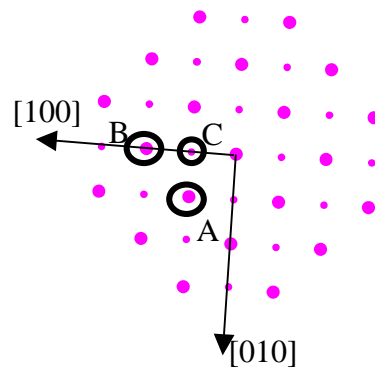
Figure 4.7 dark field images of 20at.% Ga
A:g=[110], B:g=[200], C:g=[100]

Geometry of
{001} plane

A: g=[110]

A[110]

B: g=[200]

B[200]

C: g=[100]

Geometry of
{001} plane
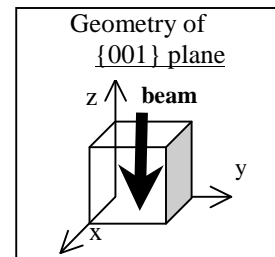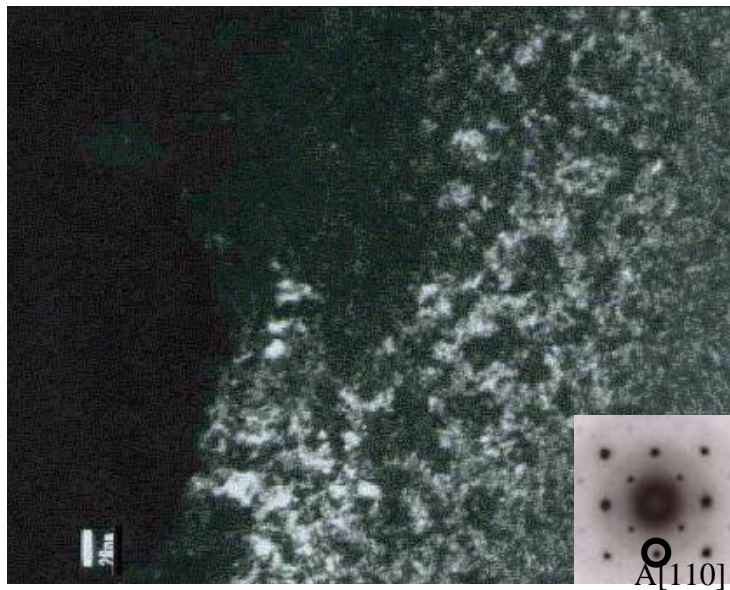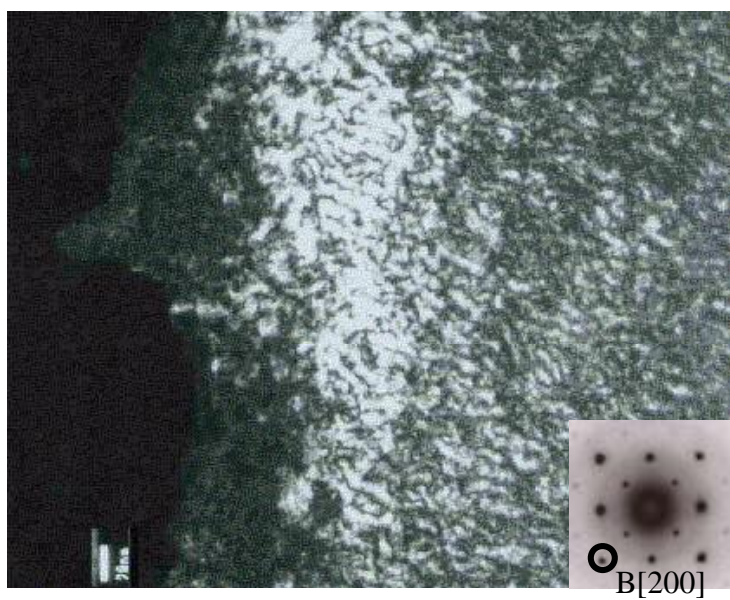
C[100]
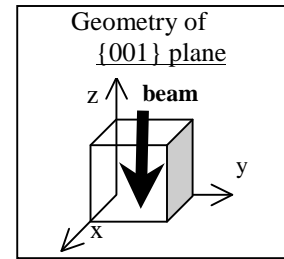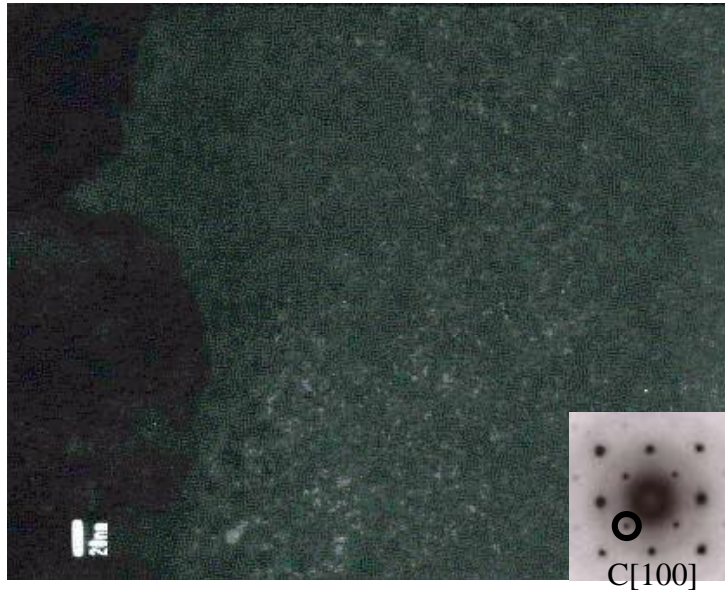
Figure 4.8 Unidentified diffraction pattern of 20at.% Ga
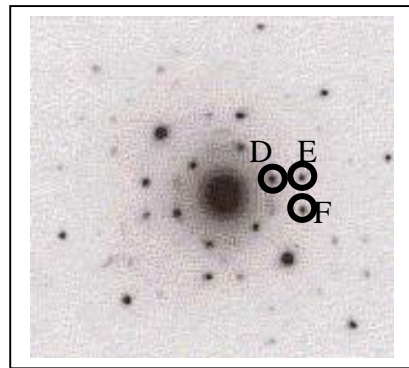
Geometry of
{$30\bar{1}$} plane

z [001]

y [010]

x [100]

Diffraction pattern of sample B-4(20at.%Ga). ◯ corresponds with unidentified spots.

<103>

(103)

D E

F

(020)

[010]

Calculated {013}-diffraction pattern of bcc (or disordered B2) structure

<103>

(206)

D E

F

(020)
(040)

[010]

Calculated {013}-diffraction pattern of DO_3 structure

<103>

(103)

D E

F

(020)

[010]
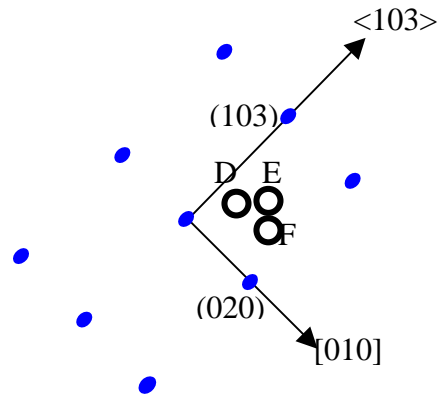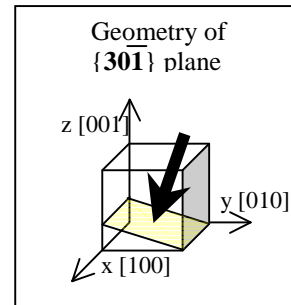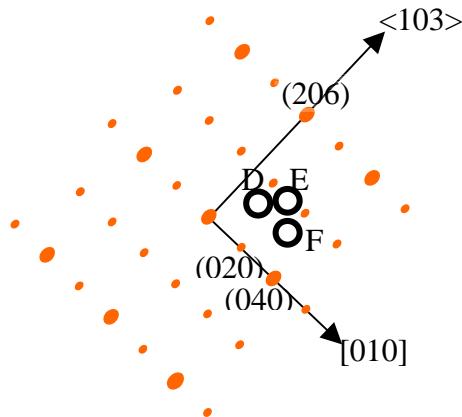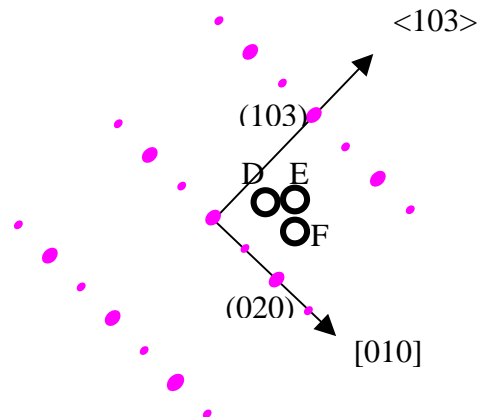
Calculated {013}-diffraction pattern of B2 structure

Figure 4.9 Dark field images of unidentified spots

D:

E:

F:

Figure 4.10 Dark field images of 14at.%Ga.
A:g=[110], B:g=[200], C:g=[100]

A: g=[110]

A[110]

B: g=[200]

B[200]

Geometry of
{001} plane

z   beam
      y
  x
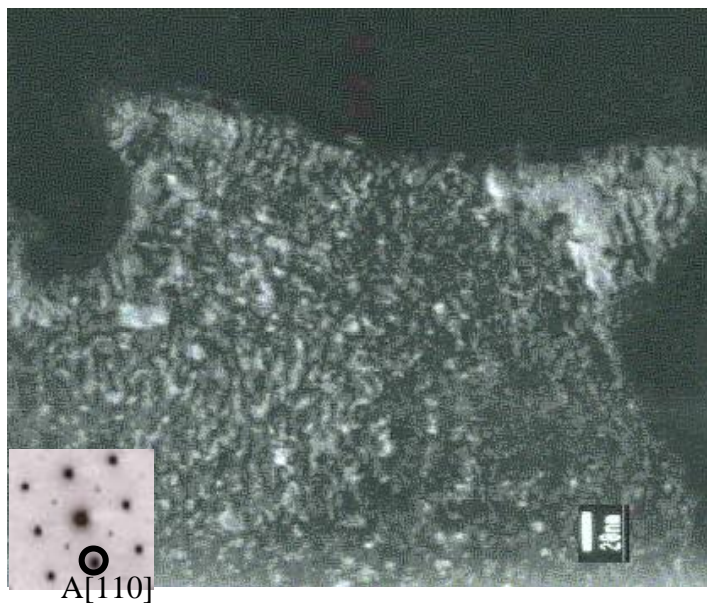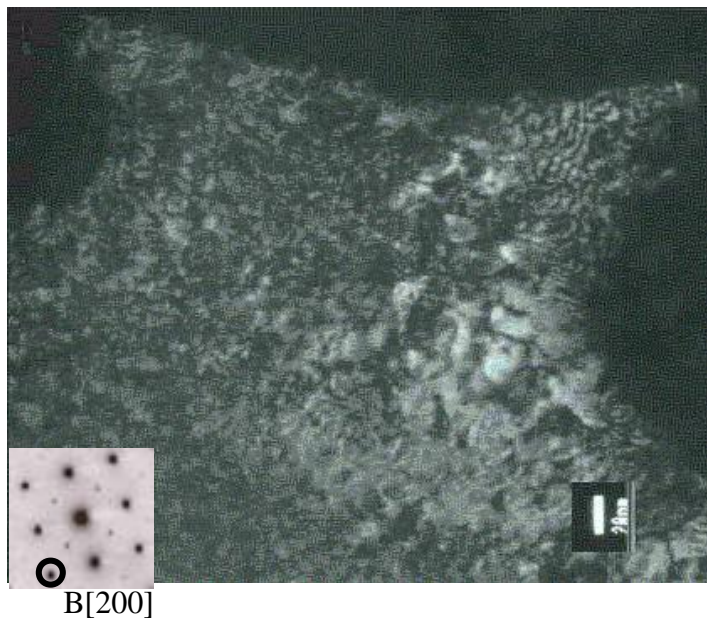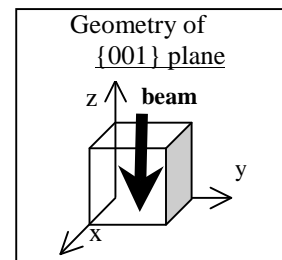
C: g=[100]

C[100]

Figure 4.11 Dark field images of 12at.%Ga.
A:g=[110], B:g=[200], C:g=[100]

Geometry of
{001} plane

z / beam
y
x

A: g=[110]

A[110]

B: g=[200]

B[200]

Geometry of
{001} plane

z beam

y

x
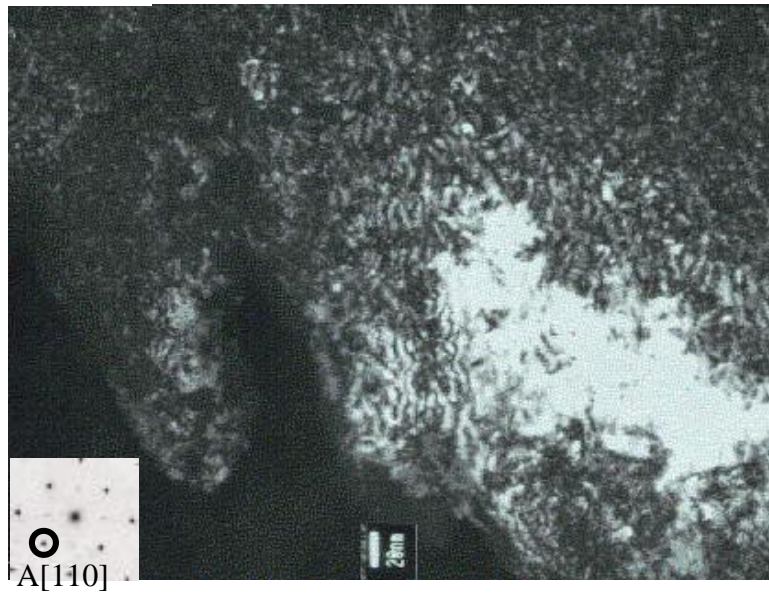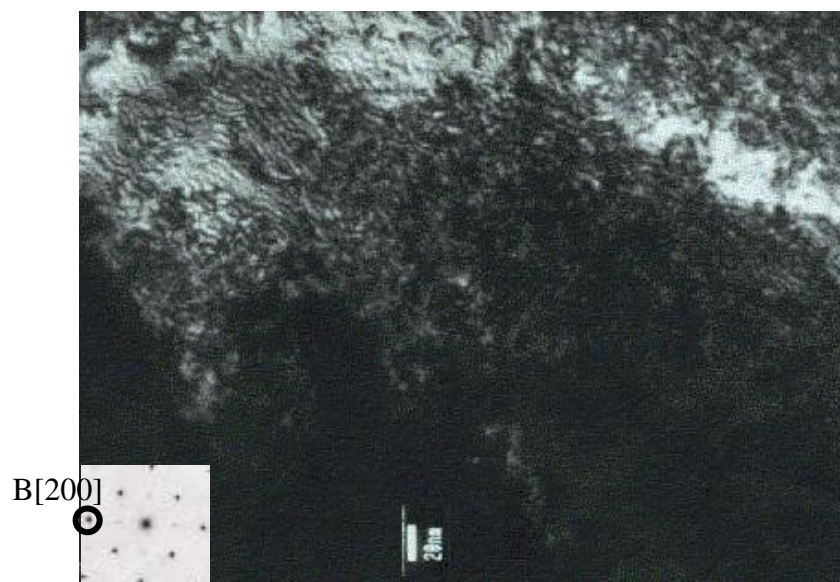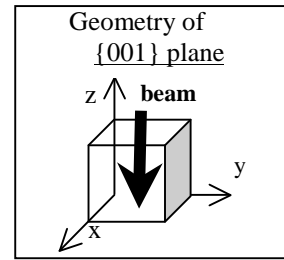
C: g=[100]

C[100]

Figure 4.12 Composition-texture correlation
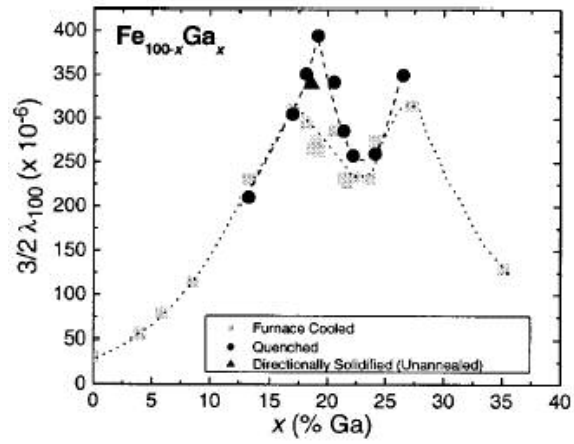
Melt-spun 17.3at.% Ga

Bulk-20at.% Ga
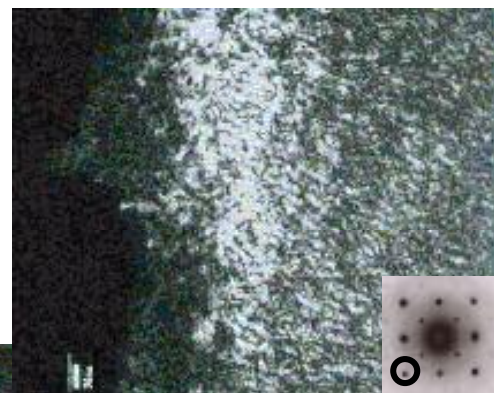
Bulk-14at.% Ga

Bulk-12at.% Ga

Geometry of
{001} plane

28
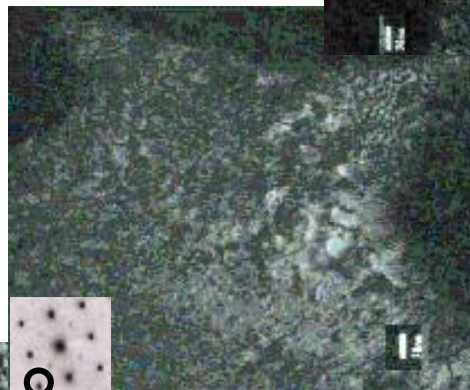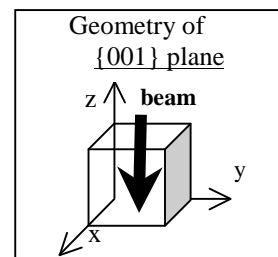
5. Discussion

5.1.　　Microstructures and Phases

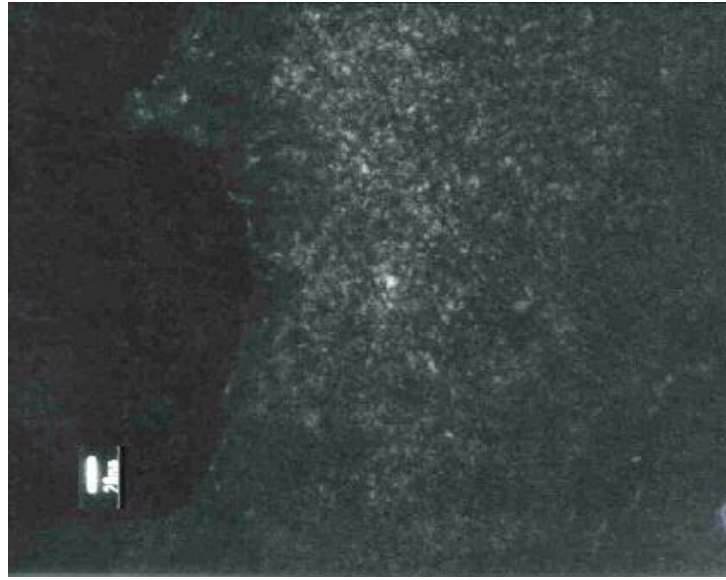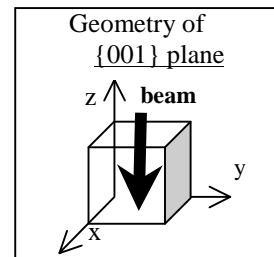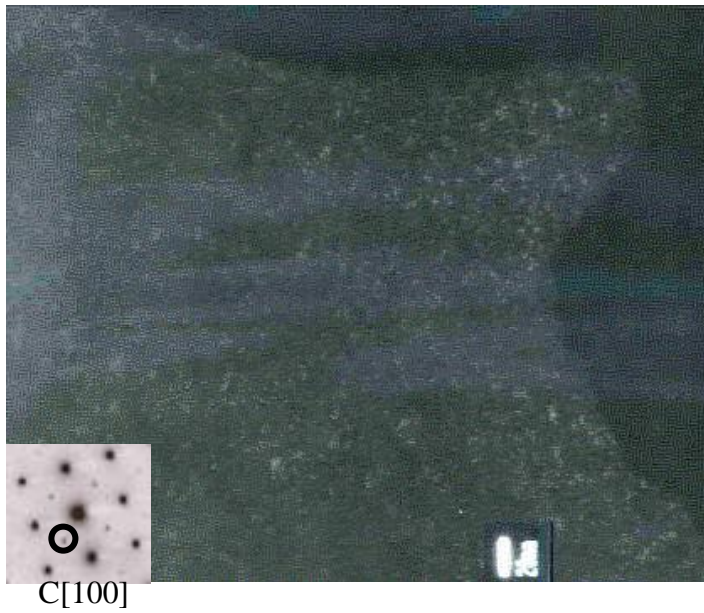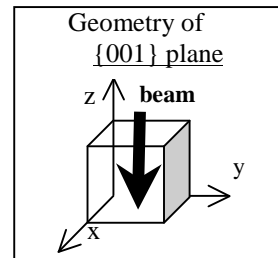### 5.1.1.　Melt-spun samples

It is clear that all the melt-spun and bulk samples have an inhomogeneous distribution of the phases or orientations. One possibility for the inhomogeneous texture seen in all the dark field images is damage from ion milling. Since it took a relatively long time for all the samples to get a hole, one can say that FeGa is a hard material to ion milling. Especially in bulk samples, which required hours of milling, the textures are more pronounced than in the melt-spun samples. In addition to that, because of the 'digging' process of milling with argon ions, it is known that some materials or elements preferentially milled. For example, it is reported InP is damaged more than GaAs[35].

Another possibility is bcc-crystal orientation itself has some inhomogeneous distribution with the order of several nanometers inside each grain (i.e. fine areas have different orientations). It is reported that this kind of <110>-orientation preference was found in annealed FeGa alloys[36].

5.1.2.　High Resolution Images

Magnified textures and crystal arrays are seen in the high resolution image (Figure 4.5). Brighter areas that look like circles are indicative of the ion milling damaging the sample because 'brighter' means 'thinner' and the size of the thinner area is too small for other mechanical damaging. Those areas contain only one of the arrays, namely the one with periodicity Δ_1 that corresponds with the lattice constant of FeGa within a margin of

error. On the other hand, the other array with Δ_2 prefers to appear in the dark areas. Note that these dark areas are also in continuous array with Δ_1. This suggests the possibility that the darker spots represent different crystal structures or additional phases with almost twice the lattice parameter of FeGa or that there are fringes caused by a layered structure.

If ion milling has a preferred of element, for example, either Fe or Ga is preferentially milled, it is reasonable to assume that the composition of FeGa alloy is locally changed, and a different crystal structure appears correspondingly. Based on the fact that Δ_2 is approximately twice Δ_1, the second phase could be the DO_3 structure with a lattice parameter twice that of the FeGa alloy. In this case, it could be suggested that the brighter area is the iron-rich phase and that it is Ga is milled away. However, if this is the case, extra spots corresponding to DO_3 with the proper orientation should appear in the diffraction pattern.

Although there are no spots can be attributed to other non-bcc structures, the bcc spots are accompanied by weak spots. These spots can be identified as a bcc structure with same the lattice constant with slightly rotated from the original coordination. Thus it is more suggestive that the array Δ_2 is not atomic planes but Moiré fringes. Moiré fringes correspond to interference between a pair of beams with slightly different g vectors, and the periodicity of the fringes is based on misfits of the lattice constants or slight rotations of the layered texture. Therefore, it could be suggested that the dark area in Figure 4.5 consists of a slightly rotated layer on top of a brighter area. Based on the fact that the array Δ_2 is found only in the darker areas, the texture observed in the dark field images could be explained as locally layered structures. However, the angle of rotation calculated from the equation $d=0.30$nm and $d_{rm}=0.56$nm gives

$$d_{rm} = \frac{d}{2\sin\beta/2}$$

where β is the angle of rotation, d is interplanar distance(0.30nm) and d_{rm} is the spacing of Moiré fringes(0.56nm), gives β=31.1° which is not consistent with the diffraction pattern[37].

These split spots are explained by Lorentz force caused by the interaction between the electron beam and the magnetization of the samples. Since the direction of Lorentz force is perpendicular to the direction of magnetization, the diffraction spots for magnetic samples can split. If this is the case, the samples can contain magnetic domains.

5.1.3. Bulk samples

Neither the contrast nor the texture of the images shows significant change corresponds to the drastic change of magnetostriction (Figure 4.12). This is consistent with the case of FeAl, which shows a similar type of texture but no specific correlation was reported [7].

On the other hand, a significant correlation is observed in the diffraction patterns. The intensity of the {001} spots in the bulk samples increases with the compositions of Ga. This suggests that the distribution of the additional phase(s) corresponds to the composition of Ga. Those spots are hardly seen in the melt-spun samples even though they are clearly observed in the bulk samples with less composition of Ga.

As discussed in the previous section, one possibility for this inhomogeneous texture is damage from ion milling. However, for the bulk samples, the existence of two-phase regions is also possible. Under equilibrium conditions, FeGa alloys with 20at.% Ga or

higher Ga composition can change into different phases, B2, DO_3, DO_{19}, $L1_2$(Fig 1.1) at lower temperatures. Therefore, it is reasonable for this sample to assume that these two-phase condition results in the inhomogenity. If this is the case, it could be suggested that these additional phases occurred from the quenching condition, and that correlates to the origin of the texture. From magnetostrictive point of view, it is reported that a bcc phase gives the largest magnetostriction [38]. Thus one can assume a 'pure' bcc FeGa phase would give the highest magnetostriction. It could be one of the reasons why large magnetostriction occurs in melt-spun samples that do not show evidence of additional phases.

However, melt-spun samples also show the fine textures. In addition to that, the dark field images taken with the <110> and <200> spots show different textures in all of the bulk and the melt-spun samples. Especially for the bulk samples, there are strong periodic textures found in all the dark field images. These results indicate that the origin of the texture is not only two (or multiple)-phase effect but also damage from ion milling.

5.2.   Tetragonal Structure

As shown in Fig.4.6, not all the diffraction spots can be identified with the structures appearing in the phase diagram. This indicates the possibility of the existence of other structures. For 20at.%, $L1_2$+ bcc phase exists below 600 C. But the calculated diffraction patterns of $L1_2$ did not agree with the obtained pattern. Another possible structure is the DO_3 whose (001)- and (20$\overline{1}$)-diffraction patterns coincide with B2.

One possibility is the existence of tetragonal structure derived from DO_3 structure[39, 40]. The crystal structure of this model is shown in figure 5.1. This crystal structure has

also been suggested explaining the undefined peaks in the x-ray diffraction spectrum [11]. From the ionic arrangement point of view, the tetragonal distortion is likely because the total energy decreases monotonically due to the ionic repulsion of Ga-atoms when this lattice is elongated along its unique axis. Also, this model is consistent with the proportionality of magnetostriction to square of alloy composition[30]. This behavior can be understood by the presence of the clusters of Ga atoms and using the pair model of magnetostriction. This supports the adjacent arrangement of same atoms in the unit cell.

Figure 5.2 shows the calculated diffraction patterns for the tetragonal structure. The lattice constant of this structure is assumed to be twice that of the bcc-Fe. Some of the spots correspond with the spots identical to the $\{20\bar{1}\}$ diffraction pattern of this structure. Although some of the spots still remain unidentified, it could be assumed that this structure is one of the reasonable assumptions.

There is a mismatch $\Delta g=(g_c-g)/g$ between the magnitude of the calculated g vector (g_c) and the obtained diffraction spots(g) (Figure 5.2). The elongation $\Delta a=(a_c-a)/a_c$ corresponds to the elongation of the crystal by 9% along <210>, <102> or <201>-direction. If this deformation is along the <102>direction, the tetragonality c/a is calculated as approximately ~1.1.

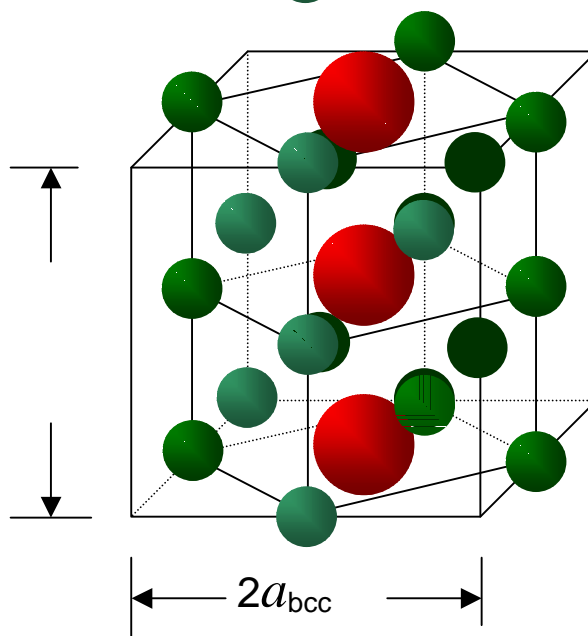Ordered DO$_3$ structure

Modulated DO$_3$ -
tetragonal structure

$2a_{bcc}$
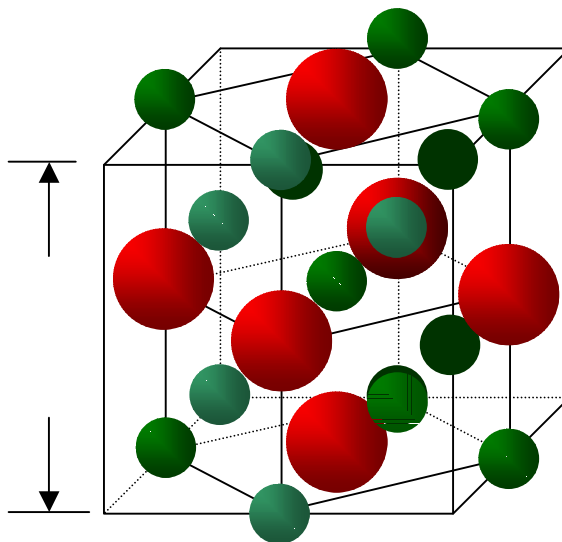
Figure 5.1 Modulated DO$_3$-tetragonal structure. :Ga, :Fe atom

34

Figure 5.2   Calculated diffraction patterns of tetragonal structure

Geometry of
{20$\bar{1}$} plane

z [001]   **e-Beam**
y [010]
x [100]

Diffraction pattern of sample B-4(20at.%Ga).   ◯ corresponds with one of the spots identical to {012} diffraction pattern.

<102>
(224)
(040)
[010]

Calculated {20$\bar{1}$}-diffraction pattern of **tetragonal** structure

O
G
G_c
Mismatch Δg

G_c: Calcaulated spot
G : Diffraction spot
$g_c = |\overrightarrow{OG_c}|$, $g = |\overrightarrow{OG}|$
$\Delta g = (g_c - g)/g$

<102>
(1$\bar{1}$2)
(020)
[010]

Calculated {20$\bar{1}$}-diffraction pattern of **bcc** structure

<102>
(224)
(040)
[010]

Calculated {20$\bar{1}$}-diffraction pattern of **DO₃** structure

5.3.   Bcc-Superlattice Structures

As discussed in the previous sections, some of the diffraction spots unidentified by the bcc or DO_3 structures are explained by modulated DO_3 tetragonal structure. On the other hand, the samples with composition of 12-16at.%-Ga in which the DO_3 and the modulation of that structure is unlikely to exist also show {001} spots. This means that there is other modulated structures correlate to bcc structure.

With considering the length of intervals of the spots, it is possible to assume the superlattices consisted of several B2 unit cells. Figure 5.4 shows the two assumptions for superlattices with the lattice parameter twice that of the as bcc-Fe. Unit-1 and -2 have one (center) and two (diagonal to each other) B2 cells, respectively, in the arrangement of every eight bcc-unit cells.

Although the simulation of those structures doesn't show a complete explanation for all the spots remained in 5.1, unit-2 shows the closest match among all of the structures discussed in the previous sections. Taking into account the unidentified spots in section 5.1, the remained spots are identified as the $\{30\overline{1}\}$-diffraction spots of unit 2.

These results show that these alloys have inhomogeneous distributions of the phases. The major structure of this sample is bcc-structure and there are modulated structures of DO_3 and/or bcc structures exist as additional phases. It should be noted that the bcc-phase as itself is inhomogeneous. The crystal structures of those additional phases are not identified precisely, however, those modulated structures of fundamental crystal structures and the structures that appeared in the phase diagrams could be the probes for the existence of the phases to explain the magnetostrictive properties.
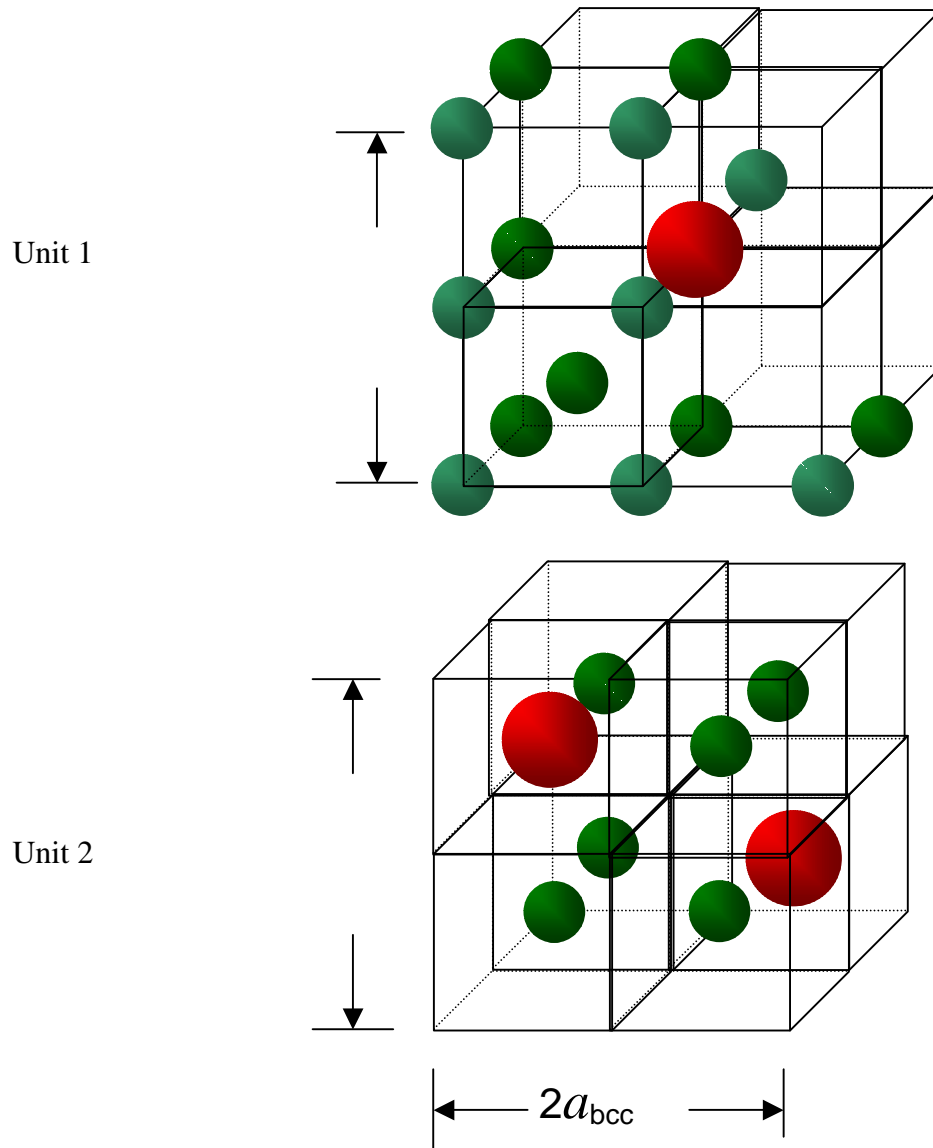
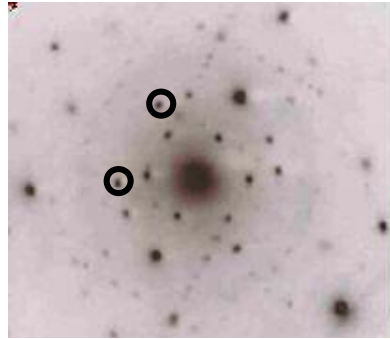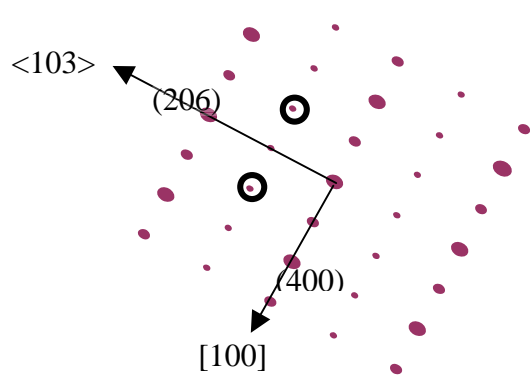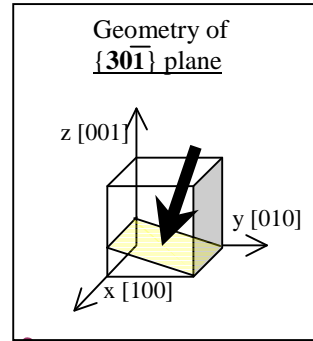Unit 1

Unit 2

$2a_{bcc}$

Figure 5.1 Figure 5.3 Assumed superlattices   :Ga,   : Fe atoms.
Unit cells consist of one (unit 1) and two (unit 2) B2 structure(s) out of 8 bcc-units.

Figure 5.4 Calculated diffraction patterns of unit 2

Geometry of
{$30\bar{1}$} plane

z [001]

y [010]

x [100]

<103>

(206)

(400)

[100]
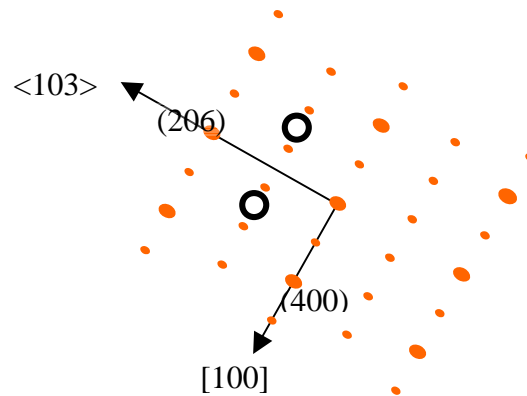
Diffraction pattern of sample B-2(14at.%Ga). **O** corresponds with unidentified spots.

Calculated {$30\bar{1}$}-diffraction pattern of **Unit-2** in figure 5.3
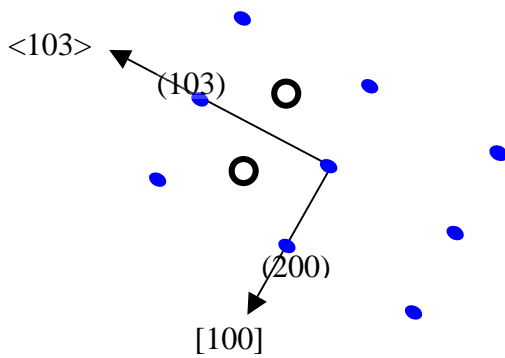
<103>

(103)

(200)

[100]

Calculated {$01\bar{3}$}-diffraction pattern of **bcc** (or disordered B2) structure

<103>

(206)

(400)

[100]

Calculated {$30\bar{1}$}-diffraction pattern of **DO₃** structure

6. Conclusion

Microstructural analysis with the transmission electron microscope was carried out for rapid-solidified (melt-spun) samples and bulk samples.

Melt-spun samples with 17.3at.%-Ga were polycrystal with bcc-crystal structure. Each domain was inhomogeneous with fine texture of 5-10nm. Dark field and high resolution image analysis suggested that the textures could due to damage from ion milling. It is also assumed that the textures consist of locally layered structure.

The bulk samples with 12-20at.%-Ga were found to have complicated microstructures. In addition to having the same type of fine textures as the melt-spun samples, they also contained additional phases other than bcc. The assumption of tetragonal modulation of DO_3 and superlattice with diagonal arrangement of two B2 cells in bcc gave the best identification for observed diffraction patterns. Mismatch between observed diffraction spots and tetragonal structure gave a 9% distortion along <102> direction.

The amount of additional phases corresponded to the composition of Ga whereas the texture didn't. Correlation between this result and the reported composition dependence of magnetostriction suggests that existence of additional phases more greatly effects the magnetostriction than the textures. On the other hand, additional phases were hardly observed in melt-spun samples. This indicates that the existence of additional phases is contributed to by the cooling rate of the alloys.

7. Future Work

In order to investigate the detail of the phases and the microtexture, one can suggest the electron energy-loss spectroscopy in a transmission electron microscope (TEM-EELS) analysis. This technique can be effective to obtain the chemical information, such as the chemical composition of the dark and bright spots in Figure 4.5. In addition to that, to find a correlation between the quenching rate in the sample preparation and the microstructure is also of high interest. This is because all the additional phases assumed in this work should not appear in ideally quenched samples.

8. Appendix I.

Basic Mechanism of Transmission Electron Microscope [41]

I-1   Basic System of TEM

Transmission Electron Microscope is a unique tool to characterize the crystal structure and the microstructure simultaneously. The crystal structure is determined by the electron diffraction and the microstructure is analyzed by the imaging. The basic diagram of the instrument is shown in Figure I-1. The incident electron beam is scattered by the specimen. Since the scattering mechanism is based on the interaction between the electron beam and the atoms of the specimen, the scattering electrons carry the information about the crystals. The information used in this work came from the diffraction patterns and the images (details are in the following section).

The first diffraction pattern appears in the back focal plane. In the diffraction mode (A), the system carries this pattern to the projection screen. In the imaging mode (B), the system carries what appeared in the intermediate image plane with magnifying the images to the screen. From this point of view, one can select a mode to see diffraction/imaging. To see the diffraction pattern, the imaging system lenses are adjusted so that the back focal plane acts as the objective lens for the intermediate lens. For imaging, one has to readjust the intermediate lens so that its object plane is the image plane of the objective lens.

Generally, a diffraction pattern observation is done before an imaging. This is because the diffraction patterns carry an important information; how the scattering is carried out.

Figure I-1 Basic diagram of transmission electron microscope
● Differaction spot,   ▽ projection of image

(A)Diffraction mode

(B)Imaging mode
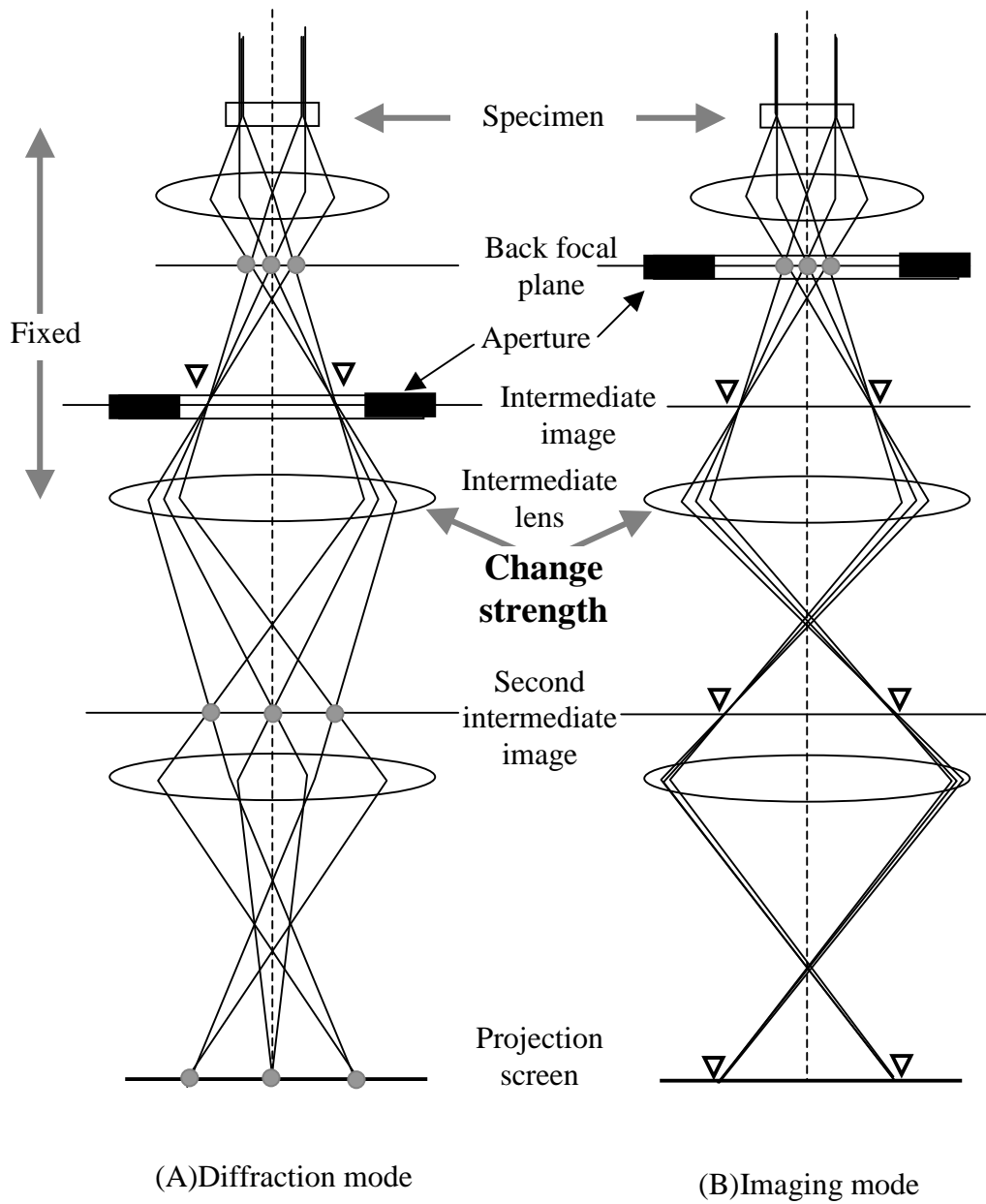
I-2 Diffractions

For a simple explanation for the electron diffraction, one can start from the Rütherford scattering. This is one of the most fundamental models of the electron scattering in the Coulombic field, in terms of 'particle' properties of electron. The differential cross section is given as

$$\frac{d\sigma(\theta)}{d\Omega} = \left(\frac{eQ}{4E_0}\right)^2 \frac{1}{\sin^4(\theta/2)}$$

where

E_0: the energy of electrons, 300keV for this work

e: charge of an electron, Q: charge of nucleus

θ : scattering angle

$d\Omega = 2\pi \sin d\theta$: solid angle element between θ and $\theta+d\theta$ [42].

Since the scattering cross section σ is a description (with unit of area) of a number of electrons scattered by Coulombic repulsive force, a physical meaning of differential cross section is understood as one of the descriptions of the amount of the scattered electrons per unit solid angle. In other words, this amount corresponds to the square of scattering amplitude of the wave function of electron propagation $f(\theta)$ in terms of 'wave' properties of electron. The square of amplitude of the wave function means 'possibility of existence' of the electron in that condition.

The incident beam and the scattered wave are described as

$$\Psi = \Psi_0 e^{2\pi i \bar{k} \cdot \bar{r}} \qquad , \qquad \Psi_{sc} = \Psi_0 f(\theta) \frac{e^{2\pi i \bar{k} \cdot \bar{r}}}{r}$$

With considering the $\pi/2$ phase change for scattering, the expression for scattering process is

$$\Psi_{sc} = \Psi_0 \left(e^{2\pi i \vec{k} \cdot \vec{r}} + if(\theta) \frac{e^{2\pi i \vec{k} \cdot \vec{r}}}{r} \right) \qquad (I\text{-}1)$$

What we can see in the TEM is the intensity of propagated wave, which is directly related to the amplitude. This amplitude A is calculated as a possibility of existence of the electron in position $\vec{r}$. With respect to the effect of scattering wave from position $\vec{r}_i$, the amplitude is described as

$$A = \sum_i \Psi(\vec{r}) \cdot \Psi_{SC}(\vec{r}_i) , \quad \text{where } /\Psi_0/^2 = 1 \text{ (normalized)}$$

Taking the origin of $\vec{r}$ and $\vec{r}_i$ to satisfy $|\vec{r}| \sim |\vec{r}_i|$ gives

$$A = \frac{e^{2\pi i \vec{k} \cdot \vec{r}}}{r} \sum_i f(\theta) e^{2\pi i \vec{k} \cdot \vec{r}_i}$$

Here $\sum_i f(\theta) e^{2\pi i \vec{k} \cdot \vec{r}}$ in right side is called the structure factor $F(\theta)$ which is a measure of the amplitude of electron beam scattered by a crystal structure. When the atomic coordination of crystals is given as (x_i, y_i, z_i), the position $\vec{r}$ and the wave vector $\vec{k}$ are written as $\vec{r} = x_i \vec{a} + y_i \vec{b} + z_i \vec{c}$ and $\vec{k} = h\vec{a}^* + k\vec{b}^* + l\vec{c}^*$, respectively, where $\vec{a}, \vec{b}$ and $\vec{c}$ are unit-cell translations in real space, $\vec{a}^*, \vec{b}^*$ and $\vec{c}^*$ are unit-cell translations in reciprocal space and $h, k,$ and l are Miller indices. The structure factor in the Bragg condition (Figure I-2) is rewritten as

$$F_{hkl} = \sum_i f_i e^{2\pi i (hx_i + ky_i + lz_i)}$$

This is the key factor that determines which spots are appeared as a diffraction pattern. For example, for bcc structure, if we set one lattice point at (0,0,0), the other (x_i, y_i, z_i) is (1/2,1/2,1/2). Therefore, the structure factor is

$$F_{hkl} = f\left\{1 + e^{\pi i(h+k+l)}\right\}$$

then one can find that $F=2f$ for $h+k+l=even$, $F=0$ for $h+k+l=odd$. Because of this, <200> and <110> are allowed but <100> is not allowed in bcc structure. In case of the CsCl structure, the scattering amplitudes f are different for different atoms, thus

$$F_{hkl} = f_{Cs} + f_{Cl}e^{\pi i(h+k+l)}$$

Therefore $F=f_{Cs}+f_{Cl}$ for $h+k+l=even$, $F=f_{Cs}-f_{Cl}$ for $h+k+l=odd$. It should be noted that there is no forbidden spots in the CsCl diffraction pattern when $h+k+l=odd$, however these spots are normally less intense compared to the others. This is the basic idea for the crystal structure identification used in section 4 (Figure 4.7, for example).
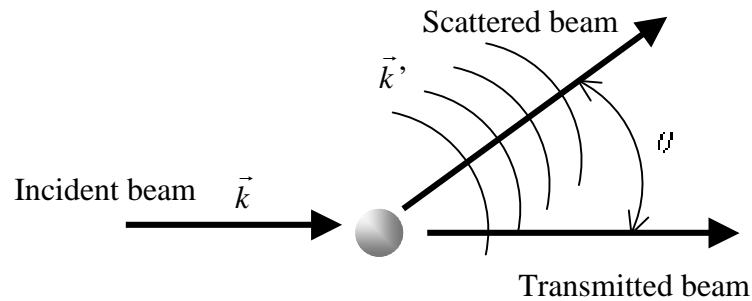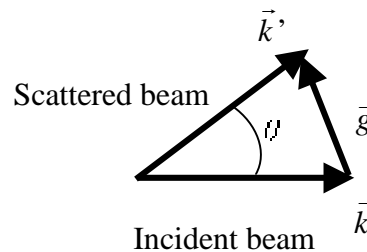
Figure I-2 Geometry of scattered wave in Bragg condition

I-3   Images

Contrast of the images come from the variation of intensities transmitted and diffracted beams due to the differences in diffraction conditions depending on the microstructural features on the electron path. When only the transmitted beam is selected, the image is called bright field imaging (BF). The contrast of this imaging is similar to optical microscope; bright area is originated by transmitted beam and dark area is not.

If one of the diffracted spots is selected by means of aperture, the image is called dark field imaging (DF). In the dark field imaging, bright area is originated by selected diffraction spot. For example, the bright areas ('texture') in Figure 4.3 came from the <110> spot. In actual observations, the off-axis electrons suffer aberrations and astigmatism and focusing the image is difficult. In order to avoid this, we adjust the system to make selected spot centered. This is called centered dark field imaging. All the dark field images in this thesis were taken with this technique.

I-4   High Resolution Images

The origin of atomic structure images in high resolution pictures is understood by means of lattice fringes produced by interference between two beams. In order to explain this, the displacement vector $\vec{s}$ (Figure I-3) is introduced. If the beam is exactly parallel to any zone axis, there should be no diffracted spots appeared because neither Bragg condition nor Laue condition is satisfied. However, in reality, a lot of diffraction spots are appeared. This means there is intensity in the diffracted beams even when the Bragg condition is not perfectly satisfied. Figure I-3 shows this 'actual' diffraction condition.

Vector $\vec{s}$ is displacement vector, which indicates the distance how far the condition is away from exact Bragg condition in reciprocal space. In this condition, the description of Bragg condition is $\vec{K} = \vec{g} + \vec{s} = \vec{k} - \vec{k}'$ instead of $\vec{K} = \vec{g} = \vec{k} - \vec{k}'$. Another expression of (I-1) is

$$\Psi = \varphi_0 \exp\{2\pi i(\vec{k} \cdot \vec{r})\} + \varphi_g \exp\{2\pi i(\vec{k}'\vec{r})\}$$

where φ_0 and φ_g are amplitude of direct and scattered beam. Substituting $\vec{k}' = \vec{k} + \vec{g} + \vec{s} = \vec{k} + \vec{g}'$, where $\vec{g}' = \vec{g} + \vec{s}$, gives

$$\Psi = \exp(2\pi i \vec{k} \cdot \vec{r})\{A + B \exp i(2\pi \vec{g}'\vec{r} + \delta)\}$$

$$\text{where} \quad \varphi_g = B \exp(i\delta)$$

$$B = \frac{\pi \sin(\pi t s)}{\xi \pi s}, \quad \text{where} \, \xi = \frac{\pi V \cos\theta}{\lambda F},$$

$$\delta = \frac{\pi}{2} - \pi s t \text{ , where } t \text{ is thickness of specimen,}$$

V is volume of unit cell and F is structure factor in Bragg condition. The intensity is

$$I = |\Psi|^2 = A^2 + B^2 + AB[\exp i(2\pi \vec{g}'\vec{r} + \delta) + \exp\{-i(2\pi \vec{g}'\vec{r} + \delta)\}]$$

$$= A^2 + B^2 + 2AB \cos(2\pi \vec{g}'\vec{r} + \delta)$$

$$= A^2 + B^2 - 2AB \sin(2\pi \vec{g}'x - \pi s t) \tag{I-2}$$

Therefore, the intensity is a sinusoidal oscillation normal to $\vec{g}'$ with a periodicity depending on s and t. If the sample is perfectly oriented as zone axis, $\vec{s} = 0$ and $\vec{g}' = \vec{g}$ are substituted into equation (I-2) then the intensity is

$$I = A^2 + B^2 - 2AB \sin(2\pi \vec{g}x)$$

Clearly this function has a periodicity in the *x* direction of *1/g* (perpendicular to $\vec{g}$') and

the magnitude equals to lattice interplaner distance *d* (Figure I-4). For many beam

condition, lattice fringes are crossing each other, and those crossover produces

arrangement of spots. It should be noted that those lattice fringes and crossing spots are,

therefore, not direct image of the structure but information about lattice spacing.

Equation (I-2) also tells us if the specimen is not exactly flat, or not perfectly

parallel to zone axis, interplaner distance is not obtained accurately from the periodicity

of fringes in high resolution image. This is why it is important for high resolution

imaging to find right area and orientation properly.

Ewalt sphere in $\vec{s}=0$

Actual Ewalt sphere

$\vec{s}$

$\vec{k}$'

Scattered beam

$\vec{g}$

Incident beam $\vec{k}$
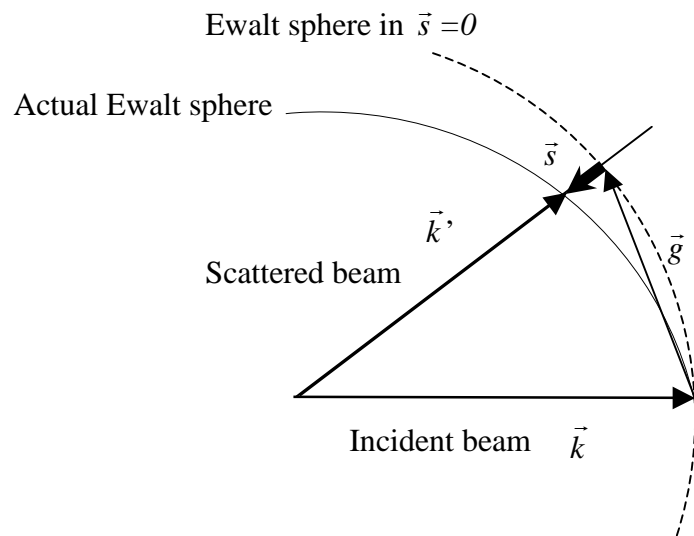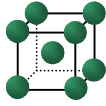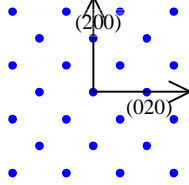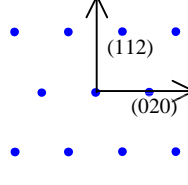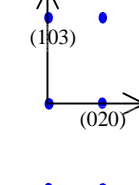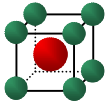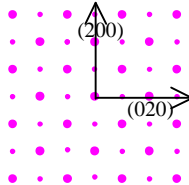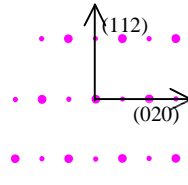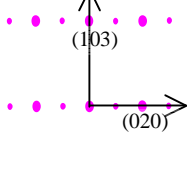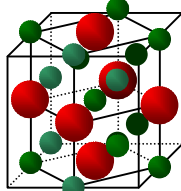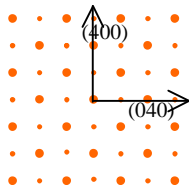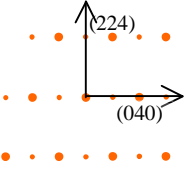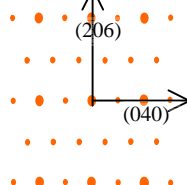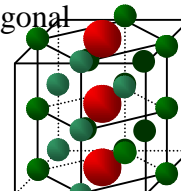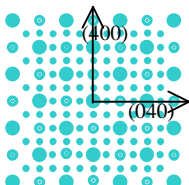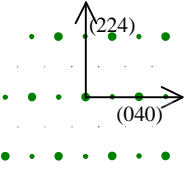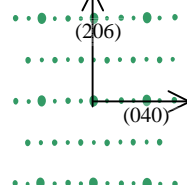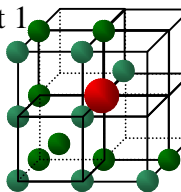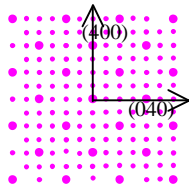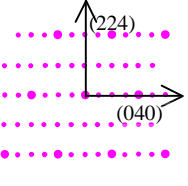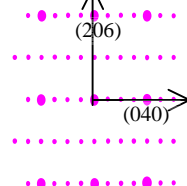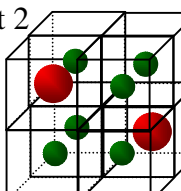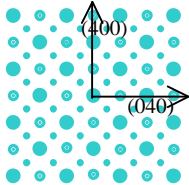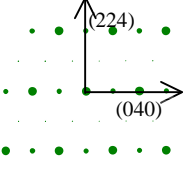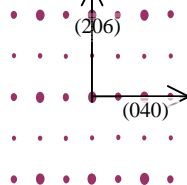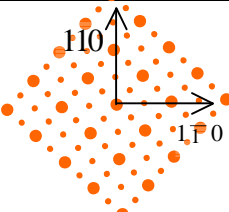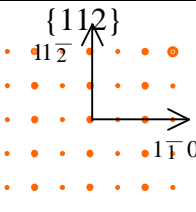
Figure I-3 Displacement from Bragg condition

Figure I-4 Schematic of lattice fringes

Reciprocal space   **Real space**

<u>Ideal two-beam condition</u>

O   G

Aperture

Diffraction spots

≚ transmitted

▪ diffracted , $\overrightarrow{OG} = \vec{g}$

d

Lattice fringes

$d = \left| \vec{g} \right|^{-1}$

Many-beam condition

O G_2

G_1

Aperture

d_2

d_1

Diffraction spots

≚ transmitted
▪ diffracted

$\overrightarrow{OG_1} = \vec{g}_1, \ \overrightarrow{OG_2} = \vec{g}_2$

Lattice fringes

$d_1 = \left| \vec{g}_1 \right|^{-1}, \ d_2 = \left| \vec{g}_2 \right|^{-1}$
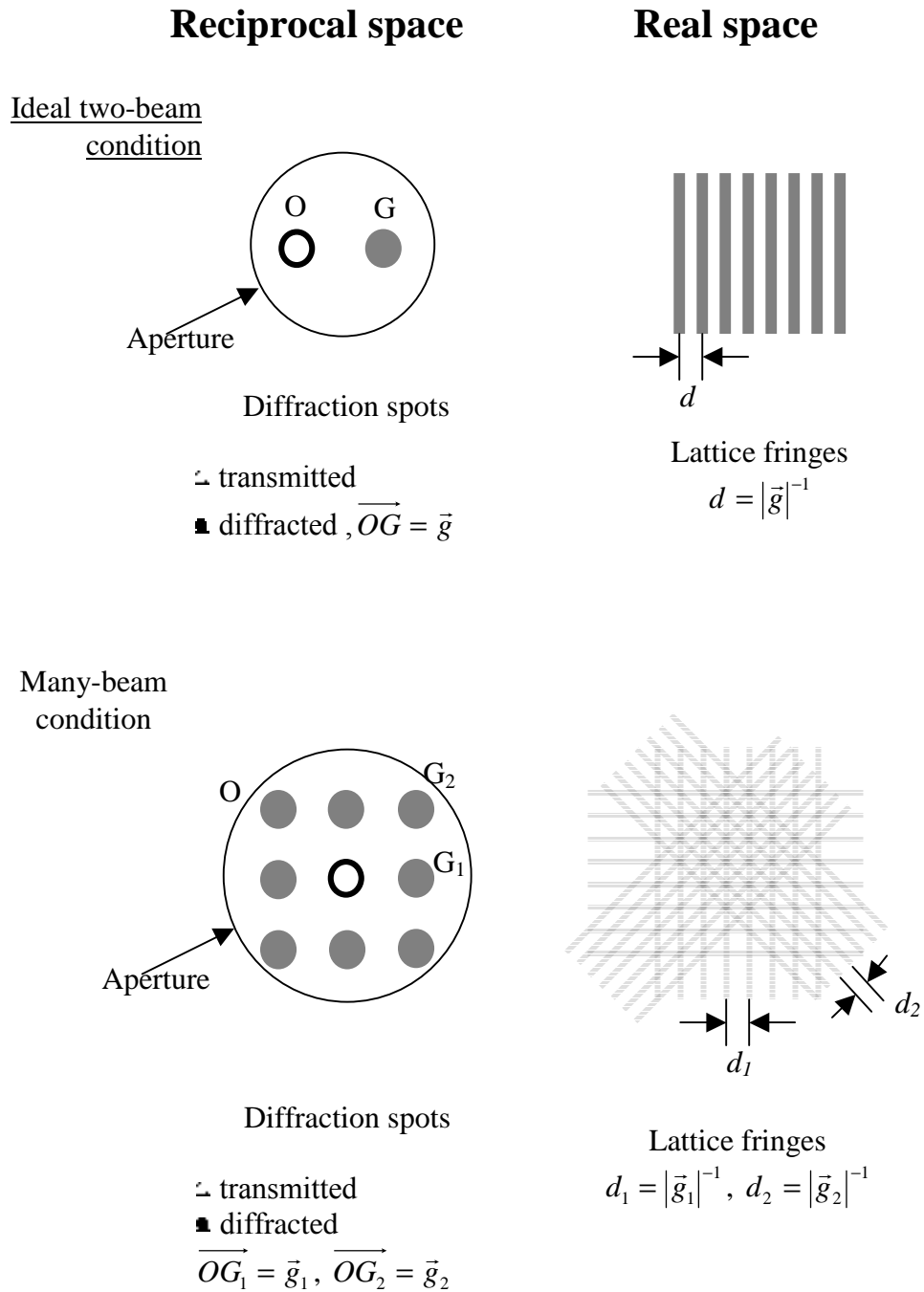
9. Appendix II. Calculated Diffraction Patterns

Crystal Structure	{001}	{102}	{103}
A2(bcc)	(200) (020)	(112) (020)	(103) (020)
B2(CsCl)	(200) (020)	(112) (020)	(103) (020)
DO$_3$	(400) (040)	(224) (040)	(206) (040)
Tetragonal	(400) (040)	(224) (040)	(206) (040)
Unit 1	(400) (040)	(224) (040)	(206) (040)
Unit 2	(400) (040)	(224) (040)	(206) (040)
L1$_2$	1̄10 1 1̄ 0	{112} 1̄1 2̄ 1 1̄ 0	

References

1. A.Taylar, R.M.Jones, J.Phys.Chem.Solids, 1958. **6**: p. 16.

2. O.Kubaschewski, *Iron-Binary Phase Diagrams*. 1982, New York.

3. R.C.Hall, J.Appl.Phys., 1957. **28**: p. 707.

4. R.C.Hall, J.Appl.Phys, 1960. **31**: p. 1037.

5. K.Nakamura, J.Phys.Soc.Japan, 1961. **16**: p. 2344.

6. H.L.Leamy, E.D.Gibson, F.X.Kayser, Acta Metall., 1967. **15**: p. 1827.

7. H.L.Leamy, Acta Metall., 1967. **15**: p. 1839.

8. A.E.Clark, J.B.Restorff, M.Wun-Fogle,T.A.Lograsso, D.L.Schlagel, IEEE Trans.Magn., 2000. **36**: p. 3238.

9. A.E.Clark, M.Wun-Fogle, J.B.Restorff, T.A.Lograsso, J.R.Cullen, IEEE Trans.Magn., 2001. **37**: p. 2678.

10. S.Guruswamy, N.Srisukhumbowornchai, A.E.Clark, J.B.Restorff, M.wun-Fogle, Scripta Mater., 2000. **43**: p. 239.

11. Y.Furuya, C.Saito, T.Okazaki, J.Japan Inst.Metals, 2002. **66**: p. 901.

12. A.E.Clark, K.B.Hathaway, M.Wun-Fogle, J.B.Restorff, T.A.Lograsso,V.M.Keppens, G.Petculescu, R.A.Taylor, J.Appl.Phys, 2003. **93**: p. 8621.

13. H.L.Luo, Trans.Met.Soc.AIME, 1967. **239**: p. 119.

14. J.R.Cullen, A.E.Clark, M.Wun-Fogle, J.B.Restorff, T.A.Lograsso, J.Magn.Magn.Mater., 2001. **226-230**: p. 948.

15. M.Wuttig, L.Dai, J.Cullen, Appl.Phys.Lett., 2002. **80**: p. 1135.

16. X.Ren, K.Otsuka, Scripta Mater., 1998. **38**(11): p. 1669.

17. S.F.Cheng, B.N.Das,M.Wun-Fogle, P.Lubitz, A.E.Clark, IEEE Trans.Magn., 2002. **38**(5): p. 2838.

18. S.Kajiwara, Mat.Sci.Eng.A, 1999. **A273-275**(-): p. 67.

19. S.Muto, R.Oshima,F.E.Fujita, Metall.Trans.A, 1988. **19A**(-): p. 2723.

20. S.Muro, R.Oshima, F.E.Fujita, Metall.Trans.A, 1988. **-**(19A): p. 2931.

21. K.Shimizu, Z.Nishizawa, Metall.Trans., 1972. **3**(-): p. 1055.

22. D.B.Williams, C.B.Carter, *Diffraction*, in *Transmission Electron Microscopy: a Textbook for Materials Science*. 1996, Plenum Press: New York. p. 259.

23. S.Muto, S.Takeda, R.Oshima, R.Oshiima, F.E.Fujita, J.J.Appl.Phys, 1988. **27**(8): p. L1387.

24. R.Oshima, S.Muto, F.E.Fujita, Mater. Trans. JIM, 1992. **33**(3): p. 197.

25. S.Muto, S.Takeda, R.Oshima, F.E.Fujita, J.Phys.Condens.Matter, 1989. **1**: p. 9971.

26. M.L.Green, M.Cohen, Acta Metall., 1979. **27**: p. 1523.

27. Xue-Wei Zhu, J.Li, M. Wuttig, Phys.Rev.B, 1991. **44**(18): p. 10367.

28. Y.Furuya, N.W.Hagwood, H.Kimura, T.Watanabe, Mater.Trans.JIM, 1998. **39**: p. 1248.

29. Y.Furuya, M.Matsumoto, H.S.Kimura, T.Masumoto, Mat.Sci.Eng.A, 1991. **A147**: p. L7.

30. T.A.Lograsso, R.A.Ross, D.L.Schlagel, A.E.Clark, M.Wun-Fogle, J.Alloys.Comp., 2003. **350**: p. 95.

31. C.Dasarathy, W.Hume-Rothery, Proc.Roy.Soc.(London), Ser.A, 1965. **286**: p. 141-157.

32. N.Kawamiya, K.Adachi, Y.Nakamura, J.Phys.Soc.Japan, 1972. **33**(-): p. 1318.

33. Jouneau, P.H., *EMS On Line Electron Microscopy Image Simulation*. 1995, Center of Interdisciplinaire de Microscopie Electronique.

34. E.Murr, L., *Electron and Ion Microscopy and Microanalysis*. Optical Engineering, ed. B. J.Thompson. 1982, New York and Basel: Marcel Dekker, Inc.

35. S.J.Pearton, U.K.Chakrabarti,A.P.Perley, J.Appl.Phys., 1990. **68**(6): p. 2760.

36. N.Srisukhumbowornchai, S.Guruswamy, J.Appl.Phys, 2001. **90**(11): p. 5680.

37. D.B.Williams, C.B.C., *Imaging*, in *Transmission Electron Microscopy: a Textbook for Materials Science*. 1996, Plenum Press: New York. p. 444-445.

38. N.Srisukhumbowornchai, S.Guruswamy, J.Appl.Phys, 2002. **92**(9): p. 5371.

39. R.Wu, J.Appl.Phys, 2002. **91**: p. 7358.

40. R.Wu, Z.Yang, J.Hong, J.Phys.:Condens.Matter, 2003. **15**: p. S587.

41. D.B.Williams, C.B.C., *Transmission Electron Microscopy: a Textbook for Materials Science*. Vol. I-IV. 1996, New York: Plenum Press.

42. K.S.Krane, *Introductory Nuclear Physics*. 1988, New York: Wiley.